Revision 1

Word count: 11258

Towards the continuous series of HgS–ZnS solid solutions: Zn-rich metacinnabar assemblages in the Vorontsovskoe gold deposit (Northern Urals, Russia)

Fedor D. Sandalov[1], Mikhail A. Rassomakhin[1], Natalia S. Vlasenko[2], Sergey N. Britvin[3], Dmitry A. Artemyev[1], Sergey Yu. Stepanov[1], Elena V. Belogub[1]

[1]South Urals Federal Research Center of Mineralogy and Geoecology of UB RAS, Miass, 456317 Russia.

[2]Centre for Geo-Environmental Research and Modelling, Saint Petersburg State University, 7/9 Universitetskaya nab., St. Petersburg, 199034 Russia.

[3]Saint Petersburg State University, 7/9 Universitetskaya nab., St. Petersburg, 199034 Russia.

Abstract

A nearly continuous series of metacinnabar–sphalerite solid solutions is reported in assemblages of Zn-rich metacinnabar in gold-bearing carbonate breccias of the Vorontsovskoe gold deposit (Northern Urals, Russia). Metacinnabar occurs as grains containing paragenetic inclusions of realgar, specific thallium-bearing sulfosalts, high-fineness native gold, and a variety of ZnS–HgS minerals, including Zn-bearing metacinnabar, Hg-bearing sphalerite, and pure cinnabar. Selected metacinnabar-sphalerite compositions fall within the $(Hg_{0.54}Zn_{0.46})S$–$(Zn_{0.62}Hg_{0.38})S$ range. This finding confirms the absence of the long-debated miscibility gap (MG), which was previously constrained to $(Hg_{0.54}Zn_{0.46})S$–$(Zn_{0.75}Hg_{0.25})S$ in the natural HgS–ZnS cubic system. The compositions obtained within the MG have the following major components ranges (wt%): Zn (17.7–27.3), Hg (50.7–63.6), S (18.7–22.0). Compositional zoning in Zn and Hg content is observed in metacinnabar. The core consists of either highly Hg-enriched sphalerite or Zn-enriched metacinnabar, while the rim is composed of low-zinc metacinnabar (3–5 wt% Zn). The Hg/Zn ratio gradually increases from core to periphery. Metacinnabar also contains minor

impurities of Mn (up to 1.2 wt%) and Cd (up to 2.6 wt%). Manganese is a nearly constant constituent. Based on published compositional data on sphalerite-metacinnabar from 38 localities, manganese is considered an indicator element for these minerals in Vorontsovskoe. Zoned zinc- and manganese-bearing metacinnabar formed during cooling (from < 350 °C to < 200 °C) of late-stage hydrothermal fluids enriched in chalcophile Tl-Cu-Zn-Hg-As-Sb-S elements. Our study suggests that a complete series of ZnS–HgS solid solutions may be found in hydrothermal systems with a relatively high-temperature formation regime (> 250 °C). Besides, Zn-Mn-bearing metacinnabar is a metastable phase in the Zn-Hg-Mn-S system. Manganese is considered a stabilizer for metacinnabar, a natural counterpart of β-HgS, which is a prospective zero-gap semiconductor.

Keywords: zincian metacinnabar; mercurian sphalerite; HgS–ZnS solid solution; Hg–Zn–Mn–S system; sulfide; Vorontsovskoe; Northern Urals; Russia

Introduction

Sphalerite and metacinnabar are isostructural cubic minerals related to the sphalerite-group MX, where M = Mn, Fe, Zn, Cd, Cu, Zn, and Hg; and X = S, Se, and Te. Other minerals in this group include browneite MnS (Ma et al. 2012), rudashevskyite (Fe,Zn)S (Britvin et al. 2008), hawleyite CdS (Traill and Boyle 1955), ishiharaite (Cu,Ga,Fe,In,Zn)S (Márquez-Zavalía et al. 2014), stilleite ZnSe (Ramdohr 1956), coloradoite HgTe (Genth 1877) and tiemannite HgSe (Naumann 1855). Sphalerite β-ZnS is the most common in nature, being a major ore mineral in polymetallic deposits. However, several polymorphs of ZnS are known to crystallize in hexagonal and trigonal crystal systems (e.g., Vasil'ev 2011).

Sphalerite is characterized by a wide range of trace and minor isomorphic impurities that substitute Zn in tetrahedral coordination. Compositions of natural sphalerite have been intensively studied as a petrogenetic indicator, given its sensitivity to ore-forming conditions (e.g., Benedetto et al. 2005; Cook et al. 2009; Frenzel et al. 2016). Cadmium, Hg, Fe and Mn commonly reach concentrations of

several weight percent in sphalerite, whereas other divalent elements, such as Co and Ni, have not been observed in considerable amounts. Zinc substitution in sphalerite follows a simple isovalent scheme: Zn^{2+} → (Cd, Hg, Fe, Mn, Co, Ni) $^{2+}$ (Cook et al. 2009; Tonkacheev et al. 2022).

Metacinnabar β-HgS (Moore 1870; Palache et al. 1944) and much more common cinnabar (trigonal α-HgS; Palache et al. 1944) are two crucial ore phases among nearly 110 Hg-defining mineral species, which contain 86 % of the metal. A hexagonal polymorph in the Hg–S system with wurtzite structure (γ-HgS, hypercinnabar) is also found in natural samples (Potter and Barnes 1978). Cinnabar (Cin) is the most stable low-temperature HgS phase, whereas pure metacinnabar (Mcin) and hypercinnabar (Hcin) are unstable at ambient conditions. The transition temperature for Cin–Mcin is suggested to be 344 ± 2 °C (Dickson and Tunnell 1959) or 345–315 °C (Potter and Barnes 1978). According to the later study (Ballirano et al. 2013), stoichiometric metacinnabar converts to cinnabar at room temperature and the rate of the conversion is quite low, reverse transition for these polymorphs seems doubtful at room conditions. For Mcin–Hcin, the transition occurs at approximately 480–470 °C established by Potter and Barnes (1978). However, the presence of impurities in metacinnabar such as Zn, Fe, Cd, Se may stabilize this high-temperature polymorph of HgS at lower temperatures (Dickson and Tunnell 1959; Boctor et al. 1987; Vasil'ev 2011; Wang et al. 2023). For hypercinnabar, Fe is the only known stabilizer (Potter and Barnes 1978). To illustrate, the presence of Fe or Zn (up to 0.3 % of each) in the metacinnabar structure lowers the inversion temperature to 305 °C and 240 °C, respectively (Dickson and Tunnell 1959). In addition, Mn doping in synthetic analogs of metacinnabar and sphalerite – both II-IV semiconductors and promising industrial materials – enhances its technologically useful physical properties (Furdyna 1988; Paszkowicz et al. 1999; Dybko et al. 1999).

Natural cubic ZnS–HgS solid solutions occur widely in various geological environments (Boctor et al. 1987; Dini et al. 1995; Powell and Pattison 1997; Cook et al. 2009; Vasil'ev 2011; Sokol et al. 2021; Wang et al. 2023). A complete series of solid solutions in the $(Zn_{1-x}Hg_x)S$ system (with $0<x<1$) has been experimentally produced at high temperature (>350 °C) by several teams (Tauson and Abramovich 1980;

Osadchii 1990; Tonkacheev et al. 2022). However, a miscibility gap has been observed in natural sphalerite-metacinnabar samples (Vasil'ev 2011; Sokol et al. 2021). The existence of a complete metacinnabar-sphalerite solid-solution series is considered doubtful (Vasil'ev 2011; Sokol et al. 2021) due to the existence of intermediate (Zn,Hg)S polhemusite with a tetragonal structure (Leonard and Desborough 1978) and miscibility rupture in the series suggested by Tauson and Abramovich (1980), Urusov (1997).

Metacinnabar, as a hypogene mineral, occurs in magmatic-related Hg-deposits (Dill 2010; Vasil'ev 2011) and more rarely in skarns and epithermal localities (Benedetto et al. 2005; Leary et al. 2016). As a supergene mineral, metacinnabar is found in the alteration zones of copper-zinc sulfide deposits (Lindgren 1933; Yakovleva et al. 2003; Belogub et al. 2008).

In the Vorontsovskoe gold deposit, a Zn-Mn-bearing metacinnabar variety has been described in low-temperature assemblages of carbonate breccias (Murzin et al. 2011, 2017; Stepanov et al. 2017; Kasatkin et al. 2022). It occurs as grains up to 0.5 cm in assemblage with carbonates (calcite, dolomite), cinnabar, coloradoite, pyrite, realgar, sphalerite, stibnite, and various sulfosalts. Sporadically, metacinnabar grains up to 0.1 mm overgrow Hg-Mn-bearing sphalerite, displaying sharp boundaries between these minerals embedded into a carbonate matrix.

In this article, we present data on zonal Zn-rich metacinnabar and Hg-rich sphalerite, its mineral assemblages, relationships between minerals of ZnS–HgS system, and discussion on formation conditions. Novel data on chemistry of metacinnabar-sphalerite series are provided. Our results were obtained using scanning electron microscopy (SEM) with both energy-dispersive X-ray (EDS) and wavelength (WDS) spectrometers, laser ablation-inductively coupled plasma-mass spectrometry (LA-ICP-MS), single X-ray diffraction (SXRD) method. Electron back-scattered diffraction (EBSD) was also applied to describe minerals of ZnS–HgS series.

Geological setting and occurrence

The Vorontsovskoe gold deposit was discovered in 1985. The deposit lies 12 km southern the Krasnoturyinsk town and 0.5 km to the West from the Vorontsovka village (59°39'5'' N 60°12'56'' E). Since 1999 to 2022 the deposit is being operated by "Northern Urals Gold" mining company (subsidiary of "Polymetall") with the ore being extracted from open-pit mines. Ore reserves of the deposit are 0.9 Moz of gold with an average grade of 2.7 ppm (Murzin et al. 2017).

The deposit is located on the eastern slope of the northern part of the Urals and belongs to the eastern part of the Tagil zone of the Tagil-Magnitogorsk megazone composed by Palaeozoic volcanic and sedimentary rocks of palaeo-ocean floor and island arc origin (Puchkov 2010; Fig. 1a). The Middle Devonian Auerbakh gabbro-diorite-granodiorite massif occurs in the southern part of the Tagil zone. The intrusive rocks of the Auerbakh massif are considered comagmatic with hosting volcanic rocks (Murzin et al. 2017).

The Vorontsovskoe deposit is located about 400–500 m from the southwestern exocontact of the Auerbakh massif (Vikent'ev et al. 2016; Fig. 1b). The deposit is hosted in volcanic-sedimentary rocks that form a monocline gently dipping westwards and plunging northwards (Murzin et al. 2017). Limestones, partially recrystallized to marbles, with layers of tuffites and siltstones (thickness of ~1 km) comprise the lithological sequence of the structure basement. Volcanic-sedimentary and volcanic rocks, tuffaceous siltstone, tuffite and tuff conformably overlain the sequence of predominantly carbonate rocks. Breccias with coarse clastic textures and tuffaceous matrix are abundant in the contact zone between these rocks and limestones. Numerous dikes, ranging compositionally from dolerites and gabbro-dolerites to diorite- and quartz-diorite porphyries, as well as lamprophyres, intrude the volcanic-sedimentary host sequence. Gold mineralization is controlled by three structural factors, including (1) horizon marker between limestone and volcanic sequences; (2) slightly inclined thrusts and associated brecciating zones; and (3) steeply dipping faults concordant with dikes (Fig. 1c).

The ore bodies mainly occur in the contact zone within brecciated limestone horizon of unclear origin (Murzin et al. 2017, and references therein). Multiple alteration styles are associated with ores: skarns, propylites, listvenites, quartz-sericite rocks, jasperoids and argillic rocks (Sazonov et al. 1998).

More than 48 ore zones have been recognized at the deposit. Four main orebodies concentrate more than 90% of reserves. The ores are divided into 3 main ore types and 6 mineral types among them. The first ore type is represented by disseminated gold-magnetite-sulfide ores in limestone skarns, gold-polymetallic ores in jasperoids and finely disseminated gold-pyrite-arsenopyrite ores in altered tuffaceous sandstones and siltstones. Of greatest economic significance and mineralogical interest is the second ore type, represented by disseminated gold-pyrite-realgar ores in carbonate breccias. Clay ores are also distinguished, which are represented by gold-sulfide ores of argillization zones and gold-oxide-clay ores of regolith.

Ore-bearing carbonate breccias are spectacular rocks composed of mainly white to orange marbleized limestone clasts with brown cement. Such breccia was formed in two stages (Stepanov et al. 2017). The first stage of brecciation produced large-block breccias of limestone with a fine-crystalline ore matrix consisting of small fragments of volcanic-sedimentary rocks with fine pyrite dissemination. The second-stage breccias include fragments of limestones, volcanogenic sedimentary rocks and siltstones. Arsenic sulfides, realgar and orpiment, are characteristic of the second-stage breccia matrix. Other minerals, such as baryte, quartz, and calcite also constitute significant parts of the matrix. Specific thallium and mercury mineralization, along with native gold, are common in this breccia type (Kasatkin et al. 2022).

Because of specific geological setting, variability of the host rocks, and ore-associated alteration, the genetic type of Vorontsovskoe is quite debatable. It exhibits features of Carlin-style, skarn, and epithermal-style deposits (Vikent'ev et al. 2016; Murzin et al. 2017; Stepanov et al. 2021). For more information on geology, genesis, and general mineralogy of the main ore bodies, as well as detailed characterization of gold-bearing breccias of the Vorontsovskoe gold deposit, refer to the following

publications: Sazonov et al. 1998; Vikent'ev et al. 2016; Murzin et al. 2017; Stepanov et al. 2017, 2021; Kasatkin et al. 2022.

Materials and methods

We examined a collection of 198 samples of carbonate ore breccia (Fig. 2), ranging in size from 5 cm to 40 cm, mined from several open pit sites of the Vorontsovskoe deposit. Samples containing rich realgar-orpiment spots and veinlets with visible inclusions of opaque sulfides and/or sulfosalts were selected for detailed investigation. A new mineral brusnitsynite $Mn_3CuPbAs_3Sb_2S_{12}$ (Kasatkin et al. 2025), which has been recently approved by the Commission of New minerals and Mineral Names of the International Mineralogical Association, was found in this rock material. Only five samples (V3, VK38a, VK38b, VK38v and VK38g), which were found to contain unusual metacinnabar grains (21 in total), were studied in detail for the purpose of this article. Descriptions of these samples and used analytical methods are given in supplemental materials (Tables S1), while data on the remaining samples will be published separately. Epoxy-mounted polished sections of the samples were prepared and investigated using the following techniques.

The back-scattered electron (BSE) images and compositions of metacinnabar and associated phases were obtained during electron microscopy study on carbon-coated samples by scanning electron microscopes Tescan Vega 3 and S-3400 N (Hitachi, Japan), equipped with an AzTec Energy X-Max 20 (Oxford Instruments, UK) EDS and an HKL NordlysNano (Oxford Instruments,UK) EBSD detector. Compositions of minerals were also determined by an JEOL JXA 8200 electron probe microanalyzer (EPMA). The analytical details, including acceleration voltage, beam current, beam diameter, analytical lines, standards, diffracting crystals and detection limits are given in Table S2.

Electron backscatter diffraction (EBSD) measurements were performed at 30 kV and 0.5–2nA. EBSD mapping was performed with 2 × 2 binning and no averaging, the exposition was 40 μsec per point. Prior to EBSD measurements, the samples were polished with progressively smaller polycrystalline

diamond suspensions with an ending step of Ar ion plasma etching for 10 min at the final stage (IonFab 300 [Oxford Instruments, UK]) to remove the amorphized layer for EBSD analysis. EBSD orientation maps were presented as color-coded images using standard techniques of colored Euler angle visualization (Euler maps, Schwartz et al. 2009). Misorientation data is presented as heatmaps, where no change in orientation in 3x3 box is depicted in blue and maximal diversion is depicted red. Diffraction contrast maps were present as monochrome images with brighter areas representing higher band contrast and local crystallinity. The structures of the phases were determined by matching the respective EBSD patterns with the reference structural models obtained from the Inorganic Crystal Structure Database (ICSD): #44365 (sphalerite), #56476 (metacinnabar), #56475 (cinnabar).

A single crystal X-ray diffraction study of metacinnabar and sulfosalts was carried out on a XCaliburS CCD diffractometer with MoKα radiation at the Center for X-Ray Diffraction Studies of the Research Park of St. Petersburg State University.

The trace element composition in metacinnabar was analyzed using a New Wave Research UP-213 laser ablation system, coupled with an Agilent 7700x (Agilent Technologies, USA) ICP-MS at the SU FRC MG UB RAS (Miass, Russia). The measurements were carried out with an Nd: YAG UV laser, frequency quadrupled (wavelength 213 nm) with fluence settings of 4.0–4.5 J/cm^2, helium cell carrier gas and a flow rate of 0.55 L/min. Mass spectrometer settings were as follows: RF Power – 1450 W; carrier gas – Ar; flow rate – 0.9L/min; plasma gas flow (Ar) – 15 L/min; auxiliary gas flow (Ar) – 0.9 L/min. Analyses were performed in ablation profiles, which were measured continuously, in inclusions-free crystal zones. Conditions were as follows: line lengths varied from 300 up to 600 μm, ablation speed 10 μm/s, a laser spot size of 80 μm diameter at a repetition rate of 10 Hz. The analyzed compositions were derived from selected stable segments of these profiles. The mass spectrometer was calibrated using NIST SRM-610. Production of molecular oxide species (i.e., $^{232}Th^{16}O/^{232}Th$) was maintained at levels below 0.3 %. The $^{238}U/^{232}Th$ ratio was kept close to unity (1:1). Data processing was carried out using the Iolite software package (Paton et al., 2011).

Elements were determined and calculated by USGS MASS-1 (Wilson et al. 2002) for several segments of each line. Limits of detection (LOD) for measured elements are given in Table S3. The dwell time was 10 ms. Zinc mean compositions obtained by EPMA were used as an internal reference using conventional approaches (Longerich et al. 1996). Due to polyatomic interferences with $^{40}Ar+^{32}S$ and $^{56}Fe+^{16}O$, ^{72}Ge values are conditional, and ^{70}Ge was not measured due to strong interference with ^{70}Zn. Quantitative LA-ICP-MS values of mercury were not reported due to its high concentrations in the grains, which resulted in an elevated analyte background.

Mineral symbols, approved by International Mineralogical Association (IMA) Commission on New Minerals, Nomenclature and Classification (CNMNC), were used (Warr, 2021).

Results

Mineral assemblages of ZnS–HgS series minerals

Metacinnabar was found in As-S-enriched spots and veinlets in ore carbonate breccia (Figs 2, 3). It occurs as individual black grains ranging from 0.2 mm up to 1.0 mm in size, closely associated with calcite, realgar, and pyrite; and less commonly with orpiment, quartz, stibnite, baryte, thallium sulfosalts – parapierrotite $TlSb_5S_8$, christite $TlHgAsS_3$, routhierite $TlCuHg_2As_2S_6$, dewitite $Ag_zTl_{10-x-z}Pb_{2x}Sb_{42-x-y}As_yS_{68}$ (with $0.00 \leq x \leq 0.40$, $16.15 \leq y \leq 19.11$, $0.04 \leq z \leq 0.11$; Topa et al. 2021), as well as coloradoite, and native gold. The obtained unit cell parameters for some sulfosalts are as follows: (1) Twinnite (P21/n) – a = 7.994(7) Å, b = 19.477(9) Å, c = 8.719(12) Å, β = 90.9 º (1), V = 1357(2) Å^3; (2) Dewitite (P-1) – a = 8.631(1) Å, b = 16.305(2) Å, c = 21.899(3) Å, α = 75.04 º (1), β = 83.61 º (1), γ = 89.04 º (1), V = 2958.7(7) Å^3. These data align well with parameters and unit cell volumes reported for these minerals by Kasatkin et al. (2022).

Most metacinnabar grains are isometric and subeuhedral, with an average size of 0.6 mm. Anhedral and deformed pseudo-flattened grains up to 1 mm crystals also occur. Some grains display simple forms of tetrahedra or hexa-tetrahedra (Fig. 2c).

Metacinnabar grains comprise numerous inclusions of associated matrix minerals, such as pyrite, realgar, calcite. Pyrite forms single dodecahedral, hexahedral, or octahedral crystals (< 50 μm) and aggregates, mainly in peripheral zones of metacinnabar grains (Fig. 3a,c). Realgar inclusions are typically round or drop-like (< 100 μm) in the marginal zones of metacinnabar and predominantly anhedral in the core zones (Fig. 4). Calcite is found near the realgar-metacinnabar grain boundaries forming saw-like intergrowth with metacinnabar (Figs 3f, 4a), which indicate synchronous growth of these two minerals. In some cases (Fig. 3g), calcite and associated realgar contain numerous submicron sphalerite inclusions, forming emulsion-like textures. Minor baryte segregations (up to 50 μm) with realgar rims are also described in metacinnabar (Fig. 3c).

The most common inclusions in metacinnabar grains are sphalerite, cinnabar, and other generations of metacinnabar, which implies a complex formation process. In reflected light, cinnabar is clearly distinguished from metacinnabar by its light grey color with a bluish tint, anisotropy, and strong red internal reflections. Three types of sphalerite (Sp1–3) and two types both of metacinnabar (Mcin1–2) and cinnabar (Cin1–2) are observed. Low-Hg sphalerite (Sp1) occurs as inclusions in the core of metacinnabar (Mcin2), while low-Zn metacinnabar (Mcin1: Figs 3d, 4) intergrowths with this sphalerite. High-Hg sphalerite (Sp2) is found in the core (Fig. 4a), and thin lamellar sphalerite (Sp3) forms myrmekite–like intergrowths with lamellar cinnabar (Cin1; Fig. 3e,f). Mcin2 is the dominant phase of metacinnabar grains, while Cin2 appears as angular, admixtures-free grains in the periphery of Mcin2, spatially associated with Cin1–Sp3 aggregates (Fig. 3h,j).

Other minor inclusions in metacinnabar include parapierrotite, christite, routhierite, coloradoite, and native gold. Thallium sulfosalts form irregular inclusions up to 50 μm in size. Notably, parapierrotite and routhierite display zoned aggregates in which Cu- and Hg-bearing routhierite is a later phase compared to parapierrotite (Fig. 3h). Native gold is of high-fineness (1000 ‰), occurring as minute inclusions (<5 μm) within thallium sulfosalts (Fig. 3h) or as grains up to 100 μm associated with anhedral metacinnabar in calcite-realgar matrix (Fig. 3i). Parapierrotite and routhierite also occur as irregular grains

in realgar matrix outside metacinnabar grains. Complex paragenetic intergrowths between parapierrotite, stibnite, realgar, and metacinnabar are observed (Fig. 3j). These relationships indicate that thallium sulfosalts were deposited first from Tl-Hg-As-Sb-S-bearing fluid, followed by eutectic-like crystallization of lamellar stibnite and realgar with minute inclusions of metacinnabar.

Assemblages lacking metacinnabar but containing ZnS-HgS minerals have been also documented. These include impurity-free cinnabar crystals (up to 100 μm) occurring as inclusions within massive Hg-Cd-Mn-bearing sphalerite, associated with realgar and an unidentified Pb-As-Sb-S sulfosalt (<20 μm). Cinnabar typically exhibits a distinct worm-like rim (<5 μm thick) interpreted as sphalerite–cinnabar diffusion boundary (Fig. 3k). Aggregates of massive pure cinnabar associated with paragenetic routhierite, christite, dewitite, and realgar are also observed (Fig. 3l). These cinnabar aggregates contains both inclusions of realgar and routhierite.

Composition of ZnS-HgS minerals: EDS, EPMA, and LA-ICP-MS data

The major and minor element compositions of minerals in the ZnS-HgS system (Sp1, Sp2, Mcin1, Mcin2, Cin2) and associated phases are provided in Tables 1, 2, and S4. A wide range of compositions in ZnS–HgS system is detected, varying from low-zinc metacinnabar (3.5 wt% Zn) to low-mercury sphalerite (2.7 wt% Hg). The composition of metacinnabar is characterized by a significant content of Zn. Mcin1 contains ~10 wt% of Zn, while Zn content in Mcin2 varies greatly (Tables 2, S4). Other admixtures in metacinnabar include Cd, up to 2.6 wt% Cd (EDS data, Table S4) or 1.2 wt% by EPMA; and Mn, up to 1.2 wt% (both EDS and EPMA data). Manganese is nearly ubiquitous in the mineral (averaging ~0.5 wt%), while cadmium is relatively rare (< 0.01 atoms per formula unit, apfu). Cadmium enrichment (>0.5 wt%) occurs exclusively in peripheral zones of some Mcin2 grains. Cinnabar-sphalerite intergrowths (Cin1–Sp3) display characteristic grid-like textures (Fig. 3e-f) with an average composition of $Hg_{0.80}Zn_{0.20}S$, which may represent the precursor composition of a high-temperature (Hg,Zn)S solid

274 solution prior to exsolution. Cinnabar crystals (Cin2) are chemically pure, corresponding to the
275 stoichiometric formula HgS.

276 Sphalerite contains Mn (1.1 wt%) and Cd (0.6 wt%) as minor constituents, similar to
277 metacinnabar. Notably, Cd was detected only in two analyses of Sp1 inclusions. These sphalerite
278 inclusions show Hg depletion and approximately two-fold Zn enrichment compared to core sphalerite
279 (Sp2). EPMA analyses reveal minor Fe impurities (0.1 wt.%, <0.01 apfu) in the sphalerite-metacinnabar
280 series.

281 The internal structure of all metacinnabar grains is strongly inhomogeneous (Figs 3 and 4). Most
282 metacinnabar grains are chemically zoned (Figs 5a-d and 6a-d): cores are strongly enriched in Zn and
283 consist of high-zinc metacinnabar or high-mercury sphalerite, while rims are relatively Zn-poor (Zn
284 content of only a few wt%). Sphalerite cores are observed only in two metacinnabar grains, possibly due
285 to random sectioning during sample preparation. No Mn or Cd zonation is found. However, Mn is
286 consistently present in all zoned samples, particularly in those containing sphalerite cores or approaching
287 intermediate (Hg,Zn)S compositions (Table 2). In these zoned grains, a nearly continuous solid solution in
288 the metacinnabar-sphalerite system has been documented for the first time in nature.

289 LA-ICP-MS compositional data on three zoned metacinnabar grains (Figs. 3c and 4a-b), calculated
290 from four ablation profiles, are given in Table 3. The concentrations of major impurities (Mn, Cd) and Fe
291 are in good agreement with both EDS and EPMA results. Trace elements (As, Tl, Cu, Sb, Se, Te) and
292 other elements in low concentrations (<100 ppm: In, Pb, Sn, Ga, Bi, Ag, Au) were also detected. The
293 distribution patterns of these constituents are generally uneven.

294 Iron is present at relatively high (up to 1243 ppm) concentrations compared to other trace
295 elements, being consistent with its role as a common isomorphic impurity in sphalerite-metacinnabar
296 minerals (Boctor et al. 1987; Cook et al. 2009).

297 Arsenic, Tl, Cu, and Sb spikes clearly observed on ablation profiles (Fig. 5) are probably
298 associated with mineral inclusions, such as routhierite and realgar, trapped during analysis. In contrast,

major (Hg, Zn) and minor elements (Mn, Cd) display smooth concentration curves, indicating homogeneous distribution. Only Hg and Zn show a negative correlation. These distribution patterns are similar to those previously observed in sphalerite of a gold-pyrite-realgar assemblage of the Vorontsovskoe deposit (Vikent'ev et al. 2016). The profiles reveal uniformly distributed Hg, Fe, Cd, and Mn, with Fe and Hg concentrations increasing progressively from core to rim in sphalerite grains.

EBSD and SXRD data

Two representative metacinnabar grains exhibiting the described features were analyzed using the EBSD method to identify phases in ZnS–HgS system, examine the inner structure of the crystals and provide insights into the possible formation mechanisms of such unusual zoned grains. The typical EBSD pattern (Kikuchi bands) corresponds to the cubic modification of HgS (metacinnabar) with a mean angular deviation (MAD) of 0.63, based on 12 bands; MAD < 1º is considered reasonable. No matches with trigonal or hexagonal modifications of HgS were found.

Both grains are single crystals with minute heterophase inclusions, as evidenced by the Euler orientation mapping (Figs 6f and 7f), and very low degree of misorientation (less than < 1º, Figs 6g and 7g). However, one exhibits distinct polysynthetic twinning (twin axis [111], 60º angle), typically occurring in cubic minerals of ZnS-HgS series (Bodshtedt-Kupletskaya and Chukhrov 1960; Fig. 7f). We interpret the observed twinning as a deformation type, postdating the formation of zoned metacinnabar crystal. Several fractures, oriented parallel or sub-parallel to crystal elongation (Fig. 7e), are observed. These fractures likely resulted from brittle deformation of initially isometric metacinnabar crystals under stress. According to the band contrast patterns, the degree of structural perfection varies in both of zoned metacinnabar grains (Figs. 6e and 7e). Diffraction contrast diminishes from the center to the periphery, correlating with decrease in the Zn/Hg ratio from the core to the rim. The inhomogeneity of these grains is also visible in EDS elemental maps (Fig. 6a–g and 7a–g).

The presence of metacinnabar, as well as associated thallium-bearing sulfosalts, was confirmed using SXRD in 40–50 μm fragments of zoned grains extracted from polished sections. The obtained cell parameter *a* for Zn-Mn-bearing metacinnabar (F-43m) is 5.7778(2) Å, V = 192.88(1) Å^3. For only Zn-bearing metacinnabar bearing, this parameter would correspond to the composition of ~72 wt% HgS and 28 wt% ZnS, which is based on the linear dependence between the cell parameter a of cubic minerals in the ZnS–HgS system and the HgS content (Vegard`s law; Vegard 1921; Kremheller 1960; Tonkacheev et al. 2022).

Discussion

ZnS–HgS mineral system with sphalerite structure

Minerals of the ZnS–HgS cubic system, including sphalerite with medium or high Hg content and zincian metacinnabar, have been extensively studied and described in numerous deposits. These include both of Hg-only and Hg-bearing complex polymetallic deposits, typically associated with precious metals mineralization (Gruzdev 1975; Vasil'ev and Lavrent'ev 1976; Boctor et al. 1987; Dini et al. 1995; Powell and Pattison 1997; Cook et al. 2009; Vasil'ev, 2011; Sokol et al. 2021; Wang et al. 2023; Kozin et al. 2024). Nevertheless, the extents of the series in natural cubic ZnS–HgS system remains unclear due to several reasons: (1) the rare occurrence of intermediate (Zn,Hg)S compositions; (2) the existence of various polymorphic and polytypic modifications for ZnS (e.g., Vasil'ev 2011) and three modifications for HgS, which may coexist within a single crystal or polycrystalline aggregate, requiring structural differentiation; (3) misidentification of HgS minerals due to application of only routine electron-microprobe methods without any X-ray diffraction or optical methods used.

Experimentally, complete miscibility in $(Zn_{1-x}Hg_x)S$ cubic system, where $0<x<1$, was observed in several studies under varying temperature and pressure conditions. Homogeneous intermediate compounds between sphalerite and metacinnabar were produced by: (1) Tauson and Abramovich (1980)

at >350 °C and 1 kbar; (2) Osadchii (1990) at 550, 700, and 800 °C under ambient pressure; (3) Tonkacheev et al. (2022) at 610–670 °C under ambient pressure.

Hence, some of these findings led to the constructions of a pseudobinary phase diagram for the Hg–Zn–S system, demonstrating complete miscibility at >350 °C (Fig. 8). At these temperatures, a high-temperature solid solution (Hss) with a sphalerite-like structure exists (Tauson and Abramovich 1980; Dini et al. 1995). As temperature decrease, two sections appear in the ZnS–HgS diagram: (1) a Hg-rich domain (~95 wt. % HgS); (2) a Zn-rich domain (~51–94 wt. % HgS). In the first case, Hss decomposes into Zn-bearing metacinnabar and Zn-free cinnabar. In the second case, two distinct solid solutions, Lss_1 (Zn-rich) and Lss_2 (Hg-rich), both with sphalerite structures, coexist. Below 200 °C, the stable paragenetic assemblage consists of Hg-sphalerite and cinnabar.

A compositional gap in the metacinnabar-sphalerite, ranging from $(Hg_{0.54}Zn_{0.46})S_{1.00}$ to $(Zn_{0.75}Hg_{0.25})S_{1.00}$, has been identified in natural samples in the metacinnabar–sphalerite series (Vasil'ev et al. 2011; Sokol et al. 2021). In calculations led to the results above, the presence of other impurities in natural samples was omitted. It is highlighted that this compositional gap in Hg-bearing sphalerite is observed in both nonzonal and zonal crystals. The former comprises Hg limits of 38 wt% in sphalerite (Gruzdev 1975), yielding the composition as follows: Zn = 37.58, Hg = 37.98, S = 24.48 wt%. The empirical formula of such sphalerite is $(Zn_{0.75}Hg_{0.25})_{1.00}S_{1.00}$. The latter varies in Hg content from 12.49 to 45.53 wt% (Dini et al. 1995). However, in zonal crystals the Hg-richest sphalerite with formula $(Zn_{0.50}Hg_{0.31}Fe_{0.12})_{0.93}(S_{1.06}Se_{0.03})_{1.07}$ contain lower Hg (by 15 wt%) than it is necessary for the intermediate member of the series (wt%: Zn = 19.80, Hg = 60.77, S = 19.43).

The compositional limit in the metacinnabar field was determined from Zn-richest metacinnabar in mercury-bearing antimony ores of B and B deposit (Idaho, USA). This metacinnabar contains 17.7 wt% Zn and corresponds to the formula $(Hg_{0.54}Zn_{0.46})_{1.00}S_{1.00}$ (Leonard and Desborough 1978). Thus, Vasil'ev (2011) concluded that the cubic ZnS–HgS series lacks solid solutions, including the intermediate member $(Hg_{0.50}Zn_{0.50})_{1.00}S$.

However, Hg-bearing sphalerite-cinnabar intergrowths with regular grid-like textures in the low-temperature Sb-As-Zn-Hg assemblage of the Hemlo Au deposit have a bulk composition of $(Hg_{0.60}Zn_{0.40})S$ (Powell and Pattison, 1997). This composition lies within suggested compositional gap and may represent the initial composition of a high-temperature homogeneous phase with a sphalerite structure. Nevertheless, data on most Hg deposits formed at < 250 °C indicate that Hg-enriched sphalerites typically coexist with Zn-metacinnabar instead of Zn-free cinnabar.

The immiscibility in cubic ZnS–HgS system has been attributed to two factors: (1) lower formation temperatures of natural Hg-enriched sphalerites compared to those in experiments, which reduces the isomorphic capacity of cubic ZnS; (2) possible structural constraints – highly Hg-enriched cubic ZnS may become unstable under ambient conditions, leading to its transformation into polhemusite.

Mercury-enriched sphalerite and Zn-enriched metacinnabar with maximum contents of 23.1 wt% Hg and 15.0 wt% Zn, respectively, has been identified in gold-bearing breccias of the Vorontsovskoe deposit (Sazonov et al. 1998; Murzin and Varlamov 2010; Murzin et al. 2011; Vikent'ev et al. 2016; Stepanov et al. 2017; Kasatkin et al. 2022). Polhemusite was also reported (Stepanov et al. 2017). However, there is no available analytical data to confirm the presence of this mineral, therefore it may represent the high-Hg variety of sphalerite.

In our study, compositions lying within $(Hg_{0.54}Zn_{0.46})S$–$(Zn_{0.75}Hg_{0.25})S$ range were obtained in zoned metacinnabar grains with sphalerite cores (some of them given in Table 2, an. 1–4; Table 3, an. 1–2; Table S4) using EDS, EPMA, and LA-ICP-MS techniques. Following the same calculation method as Vasil'ev (2011), and after excluding the presence of other impurities, the compositions were normalized to 100 % and then recalculated on the basis of 1 metal atom (Zn + Hg). The results are displayed in the diagram (Fig. 9a), showing that the gap is partially filled with compositions ranging from $(Hg_{0.54}Zn_{0.46})S$ to $(Zn_{0.62}Hg_{0.38})S$. The absence of filing in $(Zn_{0.62}Hg_{0.38})S$–$(Zn_{0.75}Hg_{0.25})S$ may result from random spotting during analysis rather than the structural transformations preventing the formation of continuous ZnS–HgS series. Calculated compositional ranges (wt%) for metacinnabar-sphalerite falling in the gap

are: Zn (17.7–27.3), Hg (50.7–63.6), S (18.7–22.0). The sphalerite-type structure of these phases is confirmed by EBSD (Figs 6f, 7f). No other distinct domains are found within the grain cores. However, cinnabar–sphalerite intergrowths (Cin1–Sp3) are observed in some peripheral regions of the crystals in elemental maps (Fig. 7b–c). Additionally, the presence of high-zinc metacinnabar (Mcin 2) is also confirmed by SXRD.

Minor elements in sphalerite–metacinnabar

Sphalerite is far more abundant in nature than its isostructural counterpart, metacinnabar; consequently, its minor and trace elements composition has been more extensively studied. Common constituents in the sphalerite structure include M^{2+} (Cd, Hg, Fe, Mn), M^{3+} (Ga, In), Ge^{4+} and Ag^{+} (Cook et al. 2009; Sokol et al. 2021). These ions, being comparable in size to Zn^{2+} in tetrahedral coordination (MS_4), demonstrate a preference for this configuration due to *sp3* hybridization (Makovicky 2006). The incorporation of Fe, Mn, Cd and Hg increases the cell parameter *a* in sphalerite, as the ionic radii for Fe^{2+}(0.77 Å), Mn (0.80 Å), Cd (0.92 Å) and Hg (1. 1 Å) exceed that of Zn^{2+}(0.74 Å) (Cordero et al. 2008).

Zinc, Cd, and Hg are all *d*-block elements in Group 12, demonstrate structural similarities in its monosulfide compounds due to the chemical and crystal-chemical properties determined by its outer ns-electrons (Ricard and Luther 2006). The electronic structures in the valence region of ZnS, CdS, and HgS compounds are largely similar. These monosulfides – ZnS (sphalerite), CdS (hawleyite), and HgS (metacinnabar) – share identical MS_4^{6-} tetrahedral units. However, there is a trend of decreasing stabilization in metal-sulfur bonding orbitals from ZnS to CdS to HgS.

Since metacinnabar is a metastable phase under ambient conditions, it rarely occurs in nature compared to cinnabar. The stabilization of metacinnabar at temperatures below the metacinnabar–cinnabar transition temperature (345 °C) is attributed to the incorporation of impurities such as Se, Zn, and Fe (Boctor et al. 1987; Dini et al. 1995; Wang et al. 2023). Cadmium may also stabilize metacinnabar enriched with impurities, as evidenced by highly Zn-Cd-enriched metacinnabar with Cd and Zn contents >

10 wt% (of each component) found in complex Hg-bearing deposits (Vasil'ev, 2011; Kozin et al. 2024). The role of Mn as a stabilizer for natural samples is unclear due to the rarity of detectable Mn in metacinnabar. According to Bodshtedt-Kupletskay and Chukhrov (1960), Mn content in natural metacinnabar is as less than 1 % in so-called onofrite, a Se-Zn-Mn variety. Experimentally, cubic HgS in the Hg-Mn-S system can incorporate up to 37.5 mol% (~14 wt%) at 600 °C (Pajaczkowska and Rabenau 1977).

For natural sphalerite the maximum Mn content is higher – up to 13 mol% (~ 11 wt%) MnS (Tauson and Chernyshev 1981). If the Mn content exceeds this threshold, the ZnS crystal structure transforms to the wurtzite-type, or separate domains of sphalerite and wurtzite coexist, reaching 50 mol% MnS in such sphalerite (Kaneko et al. 1984). To illustrate, in manganese-enriched ores of the Uchucchacua Ag-Mn-Pb-Zn skarn deposit, Mn-bearing wurtzite $(Zn_{0.65}Mn_{0.25}Fe_{0.10})S$ is a common mineral associated with alabandite, whereas low Mn-bearing sphalerite $(Zn_{0.88}Mn_{0.07}Fe_{0.06})S$ is less abundant (Bussel et al. 1990). Exceptionally Mn-rich sphalerite with 14.5 wt% Mn was described in alabandite-rich layer in grains of 30 μm × 100 μm in size closely associated with alabandite and stannite from Santo Toribio Ag epithermal deposit, Peru (Olivo and Gibbs 2003). However, it remains unclear whether the Mn impurity is completely isomorphic or partially related to the alabandite matrix.

Zinc, and minor components such as Mn and Cd, are common impurities in specific zoned metacinnabar grains in the Vorontsovskoe deposit (Table 1–3). The distribution of these elements and Hg in minerals of metacinnabar-sphalerite series was studied on a total of 259 analyses (65 – our data, 194 – from literature: Table S4) from 38 localities worldwide (Fig. 9b-d). The Zn-Hg ratio diagram (Fig. 9b), for which impurities-included compositions were used, demonstrates that most compositions fall into either mercury- or zinc-dominated regions, except for some analyses from Vorontsovskoe (Kasatkin et al. 2022; our data) and Levigliani (Dini et al. 1995) which are close to the field of intermediate compositions. Mercury-enriched sphalerite from Levigliani contains significant Fe impurity (up to 5 wt% Fe, 0.1 apfu), therefore its compositions are found slightly below a hypothetical line $x_{(Zn)} = 1 - y_{(Hg)}$ (Fig. 9b). Mercury-

Mn-bearing sphalerite and Zn-Mn-bearing metacinnabar from Vorontsovskoe consistently contain 0.5–1 wt% Mn (0.02 apfu), however, the highest Mn content in metacinnabar from this deposit (1.7 wt% Mn, 0.05 apfu) was measured by Kasatkin et al. (2022), which is close to value of 1.2 wt% Mn (0.05 apfu) obtained by us.

For sphalerite from Vorontsovskoe, the maximum Mn content reaches up to 7.6 wt%, as measured in sphalerite inclusions (up to 70 μm) within native arsenic and arsenopyrite (Murzin et al. 2011). Notably, both Mn-bearing metacinnabar and sphalerite are predominantly associated with this deposit (Fig. 9d), suggesting that Mn may serve as an indicator element for sphalerite-metacinnabar minerals at this locality. Furthermore, Mn incorporation into Hg-enriched sphalerite may contribute to structural stabilization, preserving compositions within the miscibility gap of the cubic (Zn,Hg)S system under ambient conditions.

Cadmium impurity is rare in sphalerite-metacinnabar from Vorontsovskoe, reaching up to 2.6 wt% Cd. However, LA-ICP-MS data indicate that the mean Cd content is consistent and relatively low, up to 2480 ppm (Table 3). For natural sphalerite, the maximum Cd content is 7.96 wt% (Kadyrel` Hg occurrence, Tuva, Russia: Vasil'ev 2011). In contrast, metacinnabar typically exhibits significantly higher cadmium concentration (Fig. 9c). The richest cadmium-bearing metacinnabar (up to 19.5 wt% Cd) was recently found as inclusions in cinnabar from the Izvestka Au-Pt placer in the Middle Urals, Russia (Kozin et al. 2024). This Cd concentration is close to the maximum value experimentally determined for metacinnabar – 22.78 wt% Cd (Charbonnier and Murat 1974).

Other high-cadmium metacinnabar occurrences have been reported in some Hg deposits in Russia, displaying maximum Cd concentrations as follows: 15.6 wt% (Ulandu, Gorny Altai) and 14.1 wt% (Murzinskoe Cu-Au skarns deposit, Rudny Altai). In all cases, high-cadmium metacinnabar can be classified into two compositional varieties (as suggested by Vasil'ev 2011): (1) low-zinc (0.67–3.94 wt%), with the general formula (Hg,Cd,Zn)S; (2) high-zinc (2.2–10.8 wt% Zn), with the formula (Hg,Zn,Cd)S.

Despite of scarcity of experimental data on the Zn-Hg-Cd-S system, there is the evidence from natural samples that combined Zn and Cd substitution in metacinnabar may stabilize highly Cd-enriched metacinnabar at ambient conditions. However, no correlation between Zn and Cd was observed in our samples or in the Hg-Cd-bearing metacinnabar analyses compiled by Vasil'ev (2011).

Metacinnabar assemblages and formation conditions

The coexistence of metacinnabar, cinnabar, and/or Hg-bearing sphalerite is not a novel observation, as these assemblages are well-documented in several low-temperature Hg-containing deposits (Boctor et al. 1987; Dini et al. 1995; Powell and Pattison 1997; Wang et al. 2023; Kozin et al. 2024). Also, these phase associations have been observed in experimental studies of the (Zn)-Hg-S system (Dickson and Tunell 1959; Tauson and Abramovich 1980). However, the texturally complex relationships (Fig. 3) between metacinnabar, sphalerite, cinnabar, and its varieties, combined with its paragenetic association with rare thallium minerals and native gold, represent distinctive characteristics of the Vorontsovskoe deposit that set it apart from other known occurrences.

The carbonate gold-bearing breccias of the Vorontsovskoe deposit are of particular interest due to its mineral composition, complex low-temperature sulfide-sulfosalts assemblages, petrographic types, and formation conditions, which have been thoroughly studied (Murzin et al. 2017; Vikent'ev et al. 2016, 2018; Stepanov et al. 2017, 2021; Kasatkin et al. 2022). Murzin et al. (2017) classified carbonate breccias as a Type B1 ore, containing finely disseminated gold-pyrite-realgar mineralization. A compiled data on fluid inclusions study (Murzin et al. 2017) of carbonate of the B1 ore showed that the temperature of ore formation was lower than 260–310 °C and pressure was at near-surface conditions. Pyrite is identified as the earliest sulfide in that ore, crystallizing during the propylitic alteration stage of the rock cement. Two gold-bearing mineral assemblages formed during superimposed quartz-sericite hydrothermal alteration in breccias: an early pyrrhotite-arsenopyrite assemblage (formed at 370–300 °C) and a late orpiment-realgar assemblage (250–150 °C). The early assemblage contains Fe-As sulfides, chalcopyrite and low-impurity

sphalerite (up to 0.2 Hg wt%), while the late assemblage is characterized by the presence of As-S sulfides, Hg minerals (aktashite $Cu_6Hg_3As_4S_{12}$, metacinnabar, Hg-bearing sphalerite with up to 18 wt% Hg, coloradoite), Mn minerals (alabandite and Mn sulfosalts), thallium sulfosalts (routhierite, pierrotite, chabourneite and others), copper sulfosalts, native arsenic, and high-fineness gold. Vikent'ev et al. (2018) attributed low-temperature sulfide-sulfosalts mineralization, a type #7 ore, to the Carlin-type stage of deposit formation. The paragenesis of thallium minerals, stibnite, realgar, orpiment, and high-fineness native gold is related to the final stage of ore formation, during a temperature decline to 260–110 °C, according to assessments based on fluid inclusions study of calcite from limestone breccia of this ore type. Stepanov et al. (2017) provided additional details on the structural and textural patterns of the ore breccias, revealing its fluid-explosive nature. Considering the detailed systematic study of mineralogy of the deposit by Kasatkin et al. (2022), we attribute the metacinnabar-sphalerite assemblages to a Type B1 or type #7 ore, containing fine-disseminated gold-pyrite-realgar mineralization.

Experimental data on the crystallization conditions of As and Sb sulfides and thallium sulfosalts are also available and may be helpful for reconstruction of temperature formation regime of metacinnabar assemblages. Realgar and orpiment are known low-temperature phases with melting points of 307 °C and 315 °C, respectively (Clark 1960; Kirkinskiy et al. 1967). Below 300 °C, realgar, orpiment and stibnite are formed in various proportions in the As–S–Sb system (Dickson et al. 1975). Stibnite and parapierrotite $TlSb_5S_8$, according to Tl_2S–Sb_2S_3 phase diagram (Dickson and Radtke, 1978), crystallize in the 422 to 200 °C temperature range, with more than 80 mol% of Sb_2S_3 in the system. This observation potentially indicates crystallization conditions of stibnite and parapierrotite associated with metacinnabar in samples from Vorontsovskoe (Fig. 3j). In Sb_2S_3–As_2S_3 system (Urusov 1997), stibnite and orpiment may co-crystallize in the 50–200 °C range. Additionally, a synthetic analogue of christite is obtained below 300 °C; whereas at higher temperatures, it transforms to Hg-deficient TlHgAsS, which coexists with metacinnabar above 360 °C in a melt (Radtke et al. 1977).

Taking into consideration data above, we infer that the mineral assemblage of zoned metacinnabar-sphalerite grains, containing numerous mineral inclusions, is precipitated from late-stage hydrothermal fluids enriched with chalcophile Tl-Cu-Zn-Hg-As-Sb-S mineral-forming elements during a gradual temperature decrease from medium to low values. At the same time, formation of ZnS–HgS mineral varieties and associated minerals occurred in four sequential stages, schematically represented in Fig. 10a-d.

In the initial stage (>350 °C), the cooling of late-stage hydrothermal fluids enriched with Hg, Zn, As and S as predominant components during the crystallization process occurred. Early inclusions of euhedral pyrite and baryte were encapsulated. Calcite, occurring both as protogenetic inclusions in metacinnabar and as a paragenetic phase with saw-like intergranular boundaries, may have formed during this stage. Two sulfide-enriched fluids probably existed initially (Fig. 10a): (1) As-S- enriched and (2) Hg-Zn-S-enriched. During a temperature decrease from 350 to 300 °C (Fig. 10b), low-mercury sphalerite nuclei (Sp1) crystallized first from the second-type fluid. This is due to the preference of Zn for forming crystal phases at higher temperatures in hydrothermal systems compared to Hg (Wang et al. 2023). Zincian metacinnabar (Mcin2) likely formed as a reaction rim around sphalerite, resulting from diffusion processes between Sp1 and a Zn-depleted fluid (light gray region in Fig. 10b).

As temperature decreased steadily from 300 °C to 200 °C (Fig. 10c), the Hg-enriched sphalerite core (Sp2) formed, leading to Zn depletion in the fluid and subsequent formation of low-zincian metacinnabar (Mcin2) in peripheral zones. The gradient distribution of Zn/Hg observed in elemental maps (Figs 6a–b, 7a–b) suggests slow single crystal growth. Homogeneous distribution of impurities (Mn, Cd) in Sp2–Mcin2 may also support that, as suggested for crystallization of Cd-bearing sphalerite (Benedetto et al. 2005). Alternatively, it is not ruled out that Mcin2 may have grown epitaxially and discontinuously on Sp2 crystals, resulting in concordant crystallographic orientations.

Local enrichment of the fluid in As-S, Tl-Cu-Sb, and Au led to the crystallization of realgar, thallium sulfosalts and native gold during the third stage (Fig. 10c). Below 200 °C, cinnabar–sphalerite

545 intergrowths (Cin1–Sp3) and impurity-free cinnabar (Cin2) crystallized due to Zn-bearing metacinnabar
546 exsolution. Although certain textural features in the samples may indicate that recrystallisation occurred
547 via coupled dissolution-reprecipitation reactions, CDRR, or, less probably, solid-state diffusion, SSD
548 (Boctor 1976, 1987; Putnis 2009; Wang et al. 2023). These features include the presence of Cin1–Sp3 and
549 Cin2 only in metacinnabar marginal zones (Fig. 3b,h), preservation of Mcin2 morphology and sharp
550 boundaries between Mcin2 (representing a parent phase) and Cin1+Sp3+Cin2 (product phases). For
551 instance, CDRR were successfully used to explain the formation of cinnabar–sphalerite rim in oscillatory-
552 zoned Se-enriched metacinnabar (Wang et al. 2023). CDRR typically involve fracturing and porosity due
553 to metacinnabar-cinnabar polymorphic transition, however, these features were not actually observed in
554 the metacinnabar grains of the Vorontsovskoe deposit.
555
556 **Implications**
557 Our study reveals that complete series of ZnS–HgS solid solutions with a sphalerite-type structure
558 may be found in nature. Both strongly Zn-enriched metacinnabar and Hg-enriched sphalerite crystallize
559 from high-temperature hydrothermal fluids (> 250 ºC) enriched in Tl-Cu-Zn-Hg-As-Sb-S mineral-forming
560 elements under low-pressure conditions. These phases are particularly well-developed in sulfide-sulfosalts
561 assemblages within gold-bearing breccias of the Vorontsovskoe deposit. Notably, we identify Mn as a
562 potentially structure-stabilizing impurity in metacinnabar, which is a previously unrecognized
563 characteristic. The finding gains additional significance considering that Mn-doped β-HgS is a well-
564 studied zero-gap semiconductor (Dybko et al. 1999; Kossut et al. 2003) with established applications in
565 infrared detector technology (Paszkowicz et al. 1999). Our results may provide crucial constraints for
566 future experimental studies of the Hg-Zn-Mn-S cubic system, development of novel hydrothermal
567 synthesis methods for $Hg_{1-x-y}Zn_xMn_yS$ compounds, and design of materials with tailored electromagnetic
568 properties for advanced technological applications.
569

Acknowledgments

The authors are grateful to Associate Editor Denis Fougerouse for handling the manuscript and to three anonymous reviewers for valuable comments and recommendations that helped to improve the manuscript. We are grateful to V.I. Taskaev and E.V. Kovalchuk for EPMA analysis, and V.V. Shilovskikh for discussion and useful considerations concerning the EBSD study of the samples.

Funding

This work was supported by SU FRC MG UB RAS, state contract no. 125013101191-9. The EBSD study of samples was supported by Saint-Petersburg State University, research project no. 124032000029-9. X-ray studies were carried out at the Center for X-Ray Diffraction Research of the Science Park of St. Petersburg State University within the framework of project 125021702335-5.

584 **References**

585 Ballirano, P., Botticelli, M., and Maras, A. (2013) Thermal behaviour of cinnabar, α-HgS, and
586 the kinetics of the β-HgS (metacinnabar)→ α-HgS conversion at room temperature. European Journal
587 of Mineralogy, 25(6), 957–965.

588 Belogub, E.V., Novoselov, K.A., Yakovleva, V.A., and Spiro, B. (2008) Supergene sulphides
589 and related minerals in the supergene profiles of VHMS deposits from the South Urals. Ore geology
590 reviews, 33, 239–254.

591 Benedetto, R.D., Bernardini, G.P., Costagliola, P., Plant, D., and Vaughan, D.J. (2005)
592 Compositional zoning in sphalerite crystals. American Mineralogist, 90, 1384–1392.

593 Boctor, N. (1976). The Mercury-Selenium-Sulfur System and Its Geological Implications. Part
594 1: Phase Relations in the Mercury-Selenium-Sulfur System. Part 2: The Sulfoselenides and Sulfides of
595 Mercury: Mineralogy and Geochemistry. Ph.D. Thesis, Purdue University, West Lafayette,

596 Boctor, N.Z., Shieh, Y.N., and Kullerud, G. (1987) Mercury ores from the New Idria Mining
597 District, California: Geochemical and stable isotope studies. Geochimica et Cosmochimica Acta, 51,
598 1705–1715.

599 Bodshtedt-Kupletskaya, E.M., and Chukhrov, F.V., Ed. (1960) Minerals (Reference-Book).
600 Izd. AN SSR, Moscow, 617 (in Russian).

601 Charbonnier, N., and Murat, M. (1974) Sur la determination des diagrammes de phases a
602 temperature ambiante des sulfures mixtes appartenant aux systemes Zn–Cd–S, Zn–Hg–S, Cd–Hg–S.
603 Comptes rendus de l'Académie des Sciences, 278, 259–261.

604 Clark, L.A. (1960) The Fe-As-S system--Phase relations and applications. Economic Geology,
605 55, 1345–1381.

606 Cordero, B., Gómez, V., Platero-Prats, A.E., Revés, M., Echeverría, J., Cremades, E., Barragán
607 F., Alvarez S. (2008) Covalent radii revisited. Dalton Transactions, 21, 2832–2838.

608 Dickson, F.W., and Tunell, G. (1959) The stability relations of cinnabar and metacinnabar.
609 American Mineralogist: Journal of Earth and Planetary Materials, 44, 471–487.

610 Dickson, F.W., and Radtke, A.S. (1978) Weissbergite, $TlSbS_2$, a new mineral from the Carlin
611 gold deposit, Nevada. American Mineralogist, 63, 720–724.

612 Dickson, F.W., Radtke, A.S., Weissberg, B.G., and Heropoulos C. (1975) Solid solutions of
613 antimony, arsenic, and gold in stibnite (Sb_2S_3), orpiment (As_2S_3), and realgar (As_2S_2). Economic
614 Geology, 70, 591–594.

615 Dill, H.G. (2010). The "chessboard" classification scheme of mineral deposits: Mineralogy and
616 geology from aluminum to zirconium. Earth-Science Reviews, 100, 1–420.

617 Dini, A., Benvenuti, M., Lattanzi, P., and Tanelli, G. (1995) Mineral assemblages in the Hg-
618 Zn-(Fe)-S system at Levigliani, Tuscany, Italy. European Journal of Mineralogy, 7, 417–428.

619 Dybko, K., Szuszkiewicz, W., Palacio, F., Dynowska, E., Paszkowicz, W., and Witkowska, B.
620 (1999). Magnetic properties of zinc-blende $Hg_{1-x}Mn_xS$. Journal of magnetism and magnetic materials,
621 192, 61–66.

622 Frenzel, M., Hirsch, T., and Gutzmer, J. (2016). Gallium, germanium, indium, and other trace
623 and minor elements in sphalerite as a function of deposit type—A meta-analysis. Ore Geology
624 Reviews, 76, 52–78.

625 Furdyna, J.K. (1988) Diluted magnetic semiconductors. Journal of Applied Physics, 64,
626 R29−R64.

627 Genth, F.A. (1877) Stated meeting, October 20th, 1876. Proceedings of the American
628 Philosophical Society, 16, 287–289.

629 Gruzdev, V.S. (1975) Isomorphism of zinc and mercury in natural sphalerites and
630 metacinnabars. Doklady USSR, 225, 661–664 (in Russian).

Kaneko, S., Aoki, H., Nonaka, I., Imoto, F., and Matsumoto, K. (1983) Solid Solution and Phase Transformation in the System ZnS - MnS under Hydrothermal Conditions. Journal of the Electrochemical Society, 130, 2487.

Kasatkin, A.V., Stepanov, S.Yu., Tsyganko, M.V., Škoda, R., Nestola, F., Plášil, J., Makovicky, E., Agakhanov, A.A., and Palamarchuk, R.S. (2022) Mineralogy of the Vorontsovskoe gold deposit. Mineralogy, 8, 5–93.

Kasatkin, A.V., Plášil, J., Sandalov, F.D., Nestola, F., Škoda, R., Gurzhiy, V.V., Agakhanov, A.A., and Stepanov, S.Y. (2025) Brusnitsynite, IMA 2025-010. In: CNMNC Newsletter 85, European Journal of Mineralogy, 37, 341.

Kirkinskiy, V.A., Ryaposov, A.P., and Yakushev, V.G. (1967) Phase diagram of arsenic trisulfide at pressures up to 20 kbar. Izvestiya Akademii Nauk SSSR, Neoganicheskie Materialy, 3, 1931 (in Russian).

Kossut, J., Dobrowolski, W., Story, T. (2003) II-VI and IV-VI Diluted Magnetic Semiconductors – New Bulk Materials and Low-Dimensional Quantum Structures. In K.H.J. Busschow, Ed., Handbook of Magnetic Materials, p. 289–388. Elsevier, Amsterdam, The Netherlands.

Kozin, A.K., Stepanov, S.Yu., Palamarchuk, R.S., Korneev, A.V., and Zhdanova V.S. (2024) Morphological features and chemical composition of cinnabar and metacinnabar from various placers of the Middle Urals and its possible lode sources. Zapiski RMO, 153, 3–20 (in Russian).

Kremheller, A., Levine, A.K., and Gashurov, G. (1960) Hydrothermal Preparation of Two - Component Solid Solutions from II–VI Compounds. Journal of The Electrochemical Society, 107, 12.

Leary, S., Sillitoe, R.H., Stewart, P.W., Roa, K.J., and Nicolson, B.E. (2016) Discovery, geology, and origin of the Fruta del Norte epithermal gold-silver deposit, southeastern Ecuador. Economic Geology, 111, 1043–1072.

Leonard, B.F., and Desborough, G.A. (1978) Polhemusite, a new Hg-Zn sulfide from Idaho. American Mineralogist, 63, 1153–1161.

Lindgren, W. (1933) Mineral Deposits, 930 p McGraw-Hill Book Company, Inc., New York.

Longerich, H.P., Jackson, S.E., and Günther, D. (1996) Inter-laboratory note. Laser ablation inductively coupled plasma mass spectrometric transient signal data acquisition and analyte concentration calculation. Journal of analytical atomic spectrometry, 11, 899–904.

Makovicky, E. (2006) Crystal Structures of Sulfides and Other Chalcogenides. In D.J. Vaughan, Ed., Sulfide Mineralogy and Geochemistry, p. 7–126. De Gruyter, Berlin. doi.org/10.1515/9781501509490-0037.

Márquez-Zavalía, M.F., Galliski, M.Á., Drábek, M., Vymazalová, A., Watanabe, Y., Murakami, H., and Bernhardt, H.-J. (2014) Ishiharaite, (Cu,Ga,Fe,In,Zn)S, a new mineral from the Capillitas Mine, Northwestern Argentina. Canadian Mineralogist, 52, 969–980.

Moore, G.E. (1870). Ueber das Vorkommen des amorphen Quecksilbersulfids in der Natur. Journal für Praktische Chemie, 2, 319–329.

Murzin, V.V., and Varlamov, D.A. (2010) Gold-sulfide-sulfosalts paragenesis of minerals from breccias with siliceous fragments of the Vorontsovskoe deposit (Middle Urals). Vestnik Uralskogo otdeleniya RMO, 7, 92–100 (in Russian).

Murzin, V.V., Varlamov, D.A., and Rovnushkin, M.Yu. (2011) Assemblage of native arsenic and arsenopyrite at the Vorontsovskoe gold deposit (Northern Urals). Vestnik Uralskogo otdeleniya RMO, 8, 80–87 (in Russian).

Murzin, V.V., Naumov, E.A., Azovskova, O.B., Varlamov, D.A., Rovnushkin, M.Y., and Pirajno, F. (2017) The Vorontsovskoe Au-Hg-As ore deposit (Northern Urals, Russia): Geological setting, ore mineralogy, geochemistry, geochronology and genetic model. Ore geology reviews, 85, 271–298. doi.org/10.1016/j.oregeorev.2016.10.037

Naumann, C.F. (1855) XI. Classe. Galenoide oder Glanze. B. Selenische Glanze. 531. Selenmercur oder Tiemannit. in Elemente der Mineralogie, p. 425–425 Wilhelm Engelmann, Leipzig (in German).

Olivo, G.R., and Gibbs K. (2003) Paragenesis and mineral chemistry of alabandite (MnS) from the Ag-rich Santo Toribio epithermal deposit, Northern Peru. Mineralogical Magazine, 67, 95–102.

Osadchii, E.G. (1990). The kesterite-velikite ($Cu_2Zn_{1-x}Hg_xSnS_4$) and sphalerite-metacinnabarite ($Zn_{1-x}Hg_xS$) solid solutions in the system Cu_2SnS_3-ZnS-HgS at temperatures of 850, 700 and 500 degree C. Neues Jahrbuch für Mineralogie Monatshefte, 1, 13–34.

Palache, C., Berman, H., and Frondel, C. (1944) Dana's system of mineralogy, 7th edition, v. I. 251–255.

Paszkowicz, W., Szuszkiewicz, W., Dynowska, E., Domagała, J., Witkowska, B., Marczak, M., and Zinn, P. (1999) High-pressure–high-temperature study of $Hg_{1-x}Mn_xS$. Journal of alloys and compounds, 286, 208–212.

Paton, C., Hellstrom, J., Paul, B., Woodhead, J., Hergt J. (2011) Iolite: Freeware for the visualisation and processing of mass spectrometric data. Journal of Analytical Atomic Spectrometry, 26, 2508–2518.

Potter, R.W., and Barnes, H.L. (1978) Phase relations in the binary Hg–S. American Mineralogist, 63, 1143–1152.

Powell, W.G., and Pattison, D.R. (1997) An exsolution origin for low-temperature sulfides at the Hemlo gold deposit, Ontario, Canada. Economic Geology, 92, 569–577.

Puchkov, V.N. (2010) Geology of Urals and Cis-Urals (Actual Problems of Stratigraphy, Tectonics, Geodynamics and Metallogeny), 280 p. DesignPoligraphService, Ufa, Russia (in Russian).

Putnis, A. (2009) Mineral replacement reactions. Reviews in mineralogy and geochemistry, 70, 87–124.

Ramdohr, P. (1956) Stilleit, ein neues Mineral, nat¨urliches Zinkselenid, von Shinkolobwe. Geotektonisches Symposium zu Ehren von Hans Stille, 481–483 (in German).

Sazonov, V.N., Murzin, V.V., Grigor'ev, N.A. (1998) Vorontsovsk Gold Deposit: An Example of Carlin-type Mineralization in the Urals, Russia. Geology of Ore Deposits, 40, 139–151.

706 Schwartz, A.J., Kumar, M., Adams, B.L., and Field, D.P., Ed. (2009) Electron backscatter
707 diffraction in materials science, 403 p. Springer, New York.

708 Sokol, E.V., Kokh, S.N., Nekipelova, A.V., Abersteiner, A., Seryotkin, Y.V., Ershov, V.V.,
709 Nikitenko, O.A., and Deviatiiarova, A.S. (2021) Ge-Hg-rich sphalerite and Pb, Sb, As, Hg, and Ag
710 sulfide assemblages in mud volcanoes of Sakhalin Island, Russia: An insight into possible origin.
711 Minerals, 11, 1186. doi.org/10.3390/min11111186

712 Stepanov, S.Y., Sharpyonok, L.N., Antonov, A.V. (2017) Fluid-explosive breccia of the
713 Vorontsovskoe gold deposit (Northern Urals). Zapiski RMO, 146, 29–43 (in Russian).

714 Stepanov, S.Y., Palamarchuk, R.S., Varlamov, D.A., Kiseleva, D.V., Sharpyonok, L.N., Škoda,
715 R., and Kasatkin, A.V. (2021) The features of native gold in ore-bearing breccias with realgar-
716 orpiment cement of the Vorontsovskoe deposit (Northern Urals, Russia). Minerals, 11, 541.
717 doi.org/10.3390/min11050541

718 Tauson, V.L., and Abramovich, M.G. (1980). A Study of the System ZnS-HgS by the
719 Hydrothermal Method. Geochemistry International, 17, 117–128.

720 Tauson, V.L., and Chernyshev, L.V. (1981) Experimental studies on crystal chemistry and
721 geochemistry of zinc sulfide, 190 p. Nauka, Novosibirsk, Russia (In Russian).

722 Topa, D., Stöger, B., Kolitsch, U., Keutsch, F., Stanley, C. (2021). Dewitite, IMA 2019-098.
723 European Journal of Mineralogy, 33, 639–646.

724 Traill, R.J., and Boyle, R.W. (1955) Hawleyite, isometric cadmium sulphide, a new mineral.
725 American Mineralogist: Journal of Earth and Planetary Materials, 40, 555–559.

726 Urusov, V.S., Tauson, V.L., Akimov, V.V. (1997) Solid State Geochemistry, , 500 p. Geos,
727 Moscow (In Russian).

728 Vasil'ev, V.I. (2011) New data on the composition of metacinnabar and Hg-sphalerite with an
729 isomorphous Cd admixture. Russian Geology and Geophysics, 52, 701–708.

Vasil'ev, V.I., and Lavrent'ev, Y.G. (1976) New findings of mercury-containing sphalerites and their significance. Geologiya i Geofizika, 17, 48–53 (in Russian).

Vegard, L. (1921) Die konstitution der mischkristalle und die raumfüllung der atome. Zeitschrift für Physik, 5, 17–26.

Vikent'ev, I.V., Tyukova, E.E., Murzin, V.V., Vikent'eva, O.V., and Pavlov, L.G. (2016) Vorontsovsk gold deposit. Geology, gold modes, genesis, 204 p. Fort Dialog-Iset, Ekaterinburg, Russia (in Russian).

Vikent'ev, I.V., Tyukova, E.E., Vikent'eva, O.V., Chugaev, A.V., Dubinina, E.O., Prokofiev, V.Y., and Murzin, V.V. (2018) Vorontsovka Carlin-style gold deposit in the North Urals: Mineralogy, fluid inclusion and isotope data for genetic model. Chemical Geology, 508, 144–166. doi.org/10.1016/j.chemgeo.2018.07.020

Wang, X., Liu, J., Carranza, E.J.M., Zhai, D., Zhao, Q., Weng, G., and Zhang, B. (2023) Characteristics and formation conditions of Se-Bearing metacinnabar in the Wanshan mercury ore field, Eastern Guizhou. Minerals, 13, 173. doi.org/10.3390/min13020173

Warr, L.N. (2021) IMA–CNMNC approved mineral symbols. Mineralogical Magazine, 85, 291–320.

Wilson, S.A., Ridley, W.I., and Koenig A.E. (2002) Development of sulfide calibration standards for the laser ablation inductively-coupled plasma mass spectrometry technique. Journal of Analytical Atomic Spectrometry, 17, 406–409.

Yakovleva, V.A., Belogub, E.V., and Novoselov, K.A. (2003). Supergene iron sulpho-selenides from the Zapadno-Ozernoe copper-zinc massive sulphide deposit, South Urals, Russia: a new solid-solution series between pyrite FeS_2 and dzharkenite $FeSe_2$. Mineralogical Magazine, 67, 355–361.

754 **Figure 1.** Schematic illustration of the Vorontsovskoe deposit (simplified after Sazonov et al.
755 1998; Vikent'ev et al. 2016; Stepanov et al. 2021): (a) location on tectonic structures of the Urals, (b)
756 geological map, (c) principal cross-section. Legend for Maps (a, b): 1 – Preuralian foredeep, 2 – West
757 Uralian zone, 3 – Central Uralian zone, 4 – Tagil zone, 5 – East Uralian zone, 6 – contour of (b), 7 –
758 ophiolitic-related Ordovician rocks, 8 – Ordovican basalt-rhyolite-plagiogranite, 9 – Silurian trachybasalt-
759 trachyte; Devonian formations: 10 – volcanic-sedimentary rocks with intercalations of andesites, andesite-
760 basalts and limestones; 11 – reef limestone; 12 – volcanomictic rocks with tuff horizons of andesites and
761 andesidacites; 13 – extrusive andesites; igneous rocks of the Auerbakh intrusion: 14 – porphyritic diorites
762 and gabbro-diorites; 15 – quartz diorites, granodiorites and granites; 16 – sharp rock contacts, 17 – gradual
763 rock contacts, gradual; 18 – faults, 19 – Turyinskaya ore-magmatic system; 20 – Vorontsovsko-
764 Peshchanskaya ore-magmatic system; deposits: 21 – Vorontsovskoe gold ore deposit; 22 – copper-skarn
765 deposits, 23 – Peshchanskoe iron ore deposit. Legend for cross-section (c): 24 – Neogene-Quaternary
766 cover sediments; 25 – leached limestone; Devonian formations: 26 – limestones; 27 – tuff aleurolites,
767 tuffstones, tuff-conglomerates; 28 – andesites, tuffs and lava breccias; 29 – breccia of the 1st stage of
768 breccia formation; metasomatites: 30 – quartz-sericite-albite, 31 – quartz-sericite, 32 – berezite-listvenites,
769 chlorite-sericites; dikes: 33 – lamprophyre; 34 – diorite porphyrites; 35 – ore bodies with run-of-mine
770 grades of gold content; 36 – enriched ore pillars; 37 – areas of realgar-orpiment mineralization.
771
772 **Figure 2.** Studied samples of the Vorontsovskoe deposit: (a) a typical carbonate ore breccia; (b)
773 breccia with realgar-calcite-sulfide-sulfosalts spots; (c) metacinnabar (Mcin) and thallium sulfosalts (Tl-
774 sfs: intergrowths of routhierite, christite, parapierrotite) in a realgar-orpiment-calcite matrix (sample V3);
775 (d) a single grain of metacinnabar (black) embedded into realgar-orpiment-pyrite-calcite (sample VK38v);
776 (a, d) – polished rock fragments.
777

778 **Figure 3.** Metacinnabar (a–j) and cinnabar (k–l) in breccia assemblages of the Vorontsovskoe
779 deposit: (a–c) metacinnabar grains with inclusions of routhierite (Rtr), pyrite (Py), realgar (Rlg) and baryte
780 (Brt); (d) a deformed metacinnabar crystal with sphalerite core (Sp2) and inclusions of early metacinnabar
781 (Mcin1), sphalerite (Sp1) and christite (Cri); (e) a myrmekite-like aggregate of cinnabar (Cin1) and
782 sphalerite (Sp3) with rounded realgar inclusions; (f–g) emulsion-like inclusions of sphalerite (Sp3) in
783 calcite and realgar; (h) native gold and thallium sulfosalts inclusions (Ppie – parapierrotite) in a texturally
784 complex cinnabar-metacinnabar zone; (i) assemblage of native gold with metacinnabar (grain in picture
785 "d" is shown) in calcite-realgar matrix; (j) stibnite-realgar intergrowths in paragenesis with parapierrotite
786 and cinnabar; (k) sphalerite and cinnabar with a diffusion a diffusion intergranular boundary; (l) cinnabar
787 in paragenesis with christite (Cri), routhierite, dewitite, and realgar. Note: black background is calcite (j)
788 and epoxy (l). Sample Vk38a – h, j; VK38b – d, I; VK38g – a, b, f, g; VK38v – c, e; VK35 – k, l. This and
789 the following figure are BSE images.
790
791 **Figure 4.** Zoned metacinnabar grains in realgar–calcite matrix (a – sample V3, b – VK38v).
792 Arrows labeled 1 and 2 indicate an increase in the Hg/Zn ratio from core to rim of crystals and the
793 direction of LA-ICP-MS profiles. Spots (a,b) correspond to EPMA analyses (Table 2), apfu of Zn and Hg
794 (Tables 2, S4) are depicted (c, d) for minerals of sphalerite-metacinnabar series. Cal – calcite, Rlg –
795 realgar, Rtr – routhierite, Mcin1–2 – metacinnabar, Sp1–2 – sphalerite.
796
797 **Figure 5.** Representative LA-ICP-MS profiles for selected elements in zoned metacinnabar grains
798 along 1 and 2 profiles in Figs 4a and 4b, respectively. Elevated Tl, Cu, As contents are due to routhierite
799 micro-scale inclusion (a), while As spikes are attributed to realgar grains (b). The initial (10–45 sec) high
800 Hg content (a) is due to Hg contamination during measurements.
801

802 **Figure 6.** Distribution of elements (a–d), EBSD band contrast (e), orientation in Euler colors (f),
803 and misorientation map (g) with misorientation profile of the metacinnabar grain (Fig. 4a). Here and
804 further on the Euler-color coded maps, pixel color represents an orientation of the crystal cell and,
805 basically, the pixels of the same color are showing the areas with similar unit cell orientations within
806 EBSD map.
807
808 **Figure 7.** Distribution of elements (a–d), EBSD band contrast (e), orientation in Euler colors (f),
809 and misorientation map (g) with misorientation profile of the metacinnabar grain (Fig. 4b). Arrows in the
810 image (f) indicate differently oriented regions of the twinned crystal (twin axis [111], 60º angle), with
811 orientation of crystal cells represented as green hexahedra.
812
813 **Figure 8.** Phase diagram of the ZnS–HgS system (modified after: Tauson and Abramovich 1980;
814 Dini et al. 1995; Sokol et al. 2021). Varieties of metacinnabar (Mcin1–2), sphalerite (Sp1–3), and cinnabar
815 (Cin1–2) of the Vorontsovskoe deposit are depicted with brownish colors, considering its compositional
816 ranges. Hss – high temperature (Zn,Hg)S solid solution (sphalerite structure), $Lss_{1\text{-}2}$ – low-temperature
817 solid solution (also sphalerite structure), Hg-Sp – mercury-bearing sphalerite, Zn-Mcin – zinc-bearing
818 metacinnabar. Gray dashed line indicates the temperature of Hss decomposition (< 350 °C). See text for
819 details.
820
821 **Figure 9.** Scatter plots with Hg/Zn (a,b), Hg/Cd (c) and Hg/Mn (d) ratios in metacinnabar–
822 sphalerite minerals of Vorontsovskoe and other localities. Normalized compositions without Mn and Cd
823 are used only in (a). Dashed lines mark compositions of Hg/Zn = 1:1. Grey stripes (c,d) demonstrates the
824 values below detection limit. Brown line segments (a) mark known natural compositions (Vasil'ev 2011).
825 Legend: 1–3 – Vorontsovskoe (our data, Kasatkin et al. 2022; Murzin and Varlamov 2010); 4–5 –
826 Vasil'ev 2011 (Hg deposits and Cu-Au skarns); 6 – Wang et al. 2023, and ref. therein (Hg deposits in

827 China); 7 – Kozin et al. 2024 (Izvestka Au-Pt placer, Urals, Russia); 8 – Dini et al. 1995 (Levigliani Hg
828 deposit, Italy); 9–13 – Dickson and Tunell 1959 (Hg deposits); 14 – Boctor et al. 1987 (Hg deposit in
829 serpentinites); 15–21 – Benedetto et al. 2005 (Cu-Au skarns, hydrothermal Pb-Zn veins in granitic-like
830 aureoles, VMS deposit, epithermal Pb-Zn-Cu(AuAg) veins, Pb-Zn(Sn) skarns, Zn-Pb MVT deposits, Pb-
831 Zn-Cu skarns).
832
833 **Figure 10.** Schematic illustration of metacinnabar formation. Arrows (c) indicate the crystal
834 growth direction during the cooling. Sp1–3 – sphalerite, Mcin1–2 – metacinnabar, Cin1–2 – cinnabar, Rlg
835 – realgar, Ppie – parapierrotite, Rtr – routhierite, Cri – christite, Cal – calcite, Au – native gold.
836

This is the peer-reviewed, final accepted version for American Mineralogist, published by the Mineralogical Society of America.
The published version is subject to change. Cite as Authors (Year) Title. American Mineralogist, in press.
DOI: https://doi.org/10.2138/am-2025-9783. http://www.minsocam.org/

837 **Table 1.** Composition of sphalerite, metacinnabar (including high-Cd and high-Mn varieties),

838 cinnabar, and some associated minerals, EPMA data.

No.	1	2	3	4	5	6	7	8	9	10	11
Element	Sp1 (m)*	Sp2 (m)	Mcin1 (m)	Mcin2	Mcin2	Cin2 (m)	Ppie	Twi	Cri	Rtr	Rlg
Wt%											
Mn	0.63	0.71	0.50	-	1.23	-	-	-	0.11	-	-
Cu	-	-	-	-	-	-	-	0.15	-	6.38	-
Zn	41.30	24.59	9.76	8.02	5.85	-	-	-	-	1.06	-
Cd	0.11	0.17	0.15	1.18	0.26	-	-	-	-	-	-
Hg	30.49	53.22	73.33	73.42	77.21	85.09	-	-	34.07	40.88	-
Tl	-	-	-	-	-	-	19.51	3.47	35.64	16.22	-
Pb	-	-	-	-	-	-	0.92	31.62	-	-	-
As	-	-	-	-	-	-	3.33	9.11	11.19	11.94	70.61
Sb	-	-	-	-	-	-	51.89	30.94	1.37	4.43	-
S	25.80	20.79	16.74	15.68	15.90	13.98	24.70	24.03	16.52	19.31	30.49
Total***	98.52	99.65	100.61	98.30	100.45	99.06	100.36	99.34	98.94	100.22	101.10
Apfu**											
Mn	0.01	0.02	0.02	-	0.05	-	-	-	0.01	-	-
Cu	-	-	-	-	-	-	-	0.01	-	1.01	-
Zn	0.79	0.58	0.29	0.25	0.18	-	-	-	-	0.16	-
Cd	<0.01	<0.01	<0.01	0.02	0.01	-	-	-	-	-	-
Hg	0.19	0.41	0.70	0.74	0.77	0.99	-	-	1.00	2.04	-
Tl	-	-	-	-	-	-	1.00	0.09	1.02	0.80	-
Pb	-	-	-	-	-	-	0.05	0.82	-	-	-
As	-	-	-	-	-	-	0.47	0.66	0.88	1.60	3.98
Sb	-	-	-	-	-	-	4.45	1.37	0.07	0.36	-
S	1.00	0.99	1.00	0.99	1.00	1.01	8.04	4.04	3.02	6.03	4.02

839 *Mean (m) composition (n = 7/5/4/7). **Here and further formulas are calculated on basis of: 2 atoms –
840 Sp, Mcin and Cin; 14 – parapierrotite (Ppie); 7 – twinnite (Twi); 6 – christite (Cri); 12 – routhierite (Rtr);
841 8 – realgar (Rlg). Dash indicates values below the detection limit. ***An. 1,2,3 also include Fe (wt%,
842 apfu): 0.18 (<0.01), 0.17(0.01), and 0.13 (<0.01), respectively.

843

844

845 **Table 2.** Composition of sphalerite-metacinnabar (Sp2, Mcin2) of zonal crystals along profiles 1

846 and 2 (Fig. 4), EPMA data.

No.	Wt%							apfu					
	Mn	Fe	Zn	Cd	Hg	S	Total	Mn	Fe	Zn	Cd	Hg	S
1-1	0.75	0.15	24.77	0.15	53.06	20.83	99.71	0.02	<0.01	0.58	<0.01	0.40	0.99
1-2	0.74	0.16	23.86	0.18	53.91	20.49	99.32	0.02	<0.01	0.57	<0.01	0.42	0.99
1-3	0.92	0.16	22.86	0.16	54.75	20.35	99.21	0.03	<0.01	0.55	<0.01	0.43	0.99
1-4	0.91	0.10	19.60	0.15	59.36	19.51	99.63	0.03	<0.01	0.49	<0.01	0.48	0.99
1-5	0.79	0.13	15.49	0.12	65.04	18.39	99.96	0.03	<0.01	0.41	<0.01	0.56	1.00
1-6	0.72	-	13.26	0.11	69.00	17.61	100.70	0.02	-	0.37	<0.01	0.62	0.99
1-7	0.65	0.09	11.17	0.13	71.12	17.15	100.31	0.02	<0.01	0.32	<0.01	0.66	1.00
1-8	0.55	0.12	8.89	0.10	73.56	16.31	99.53	0.02	<0.01	0.27	<0.01	0.72	0.99
1-9	0.51	-	7.08	0.12	76.70	16.02	100.42	0.02	-	0.22	<0.01	0.76	1.00
1-10	0.49	-	5.88	0.10	78.12	15.58	100.17	0.02	-	0.18	<0.01	0.80	1.00
1-11	0.48	-	5.02	0.08	78.27	15.28	99.13	0.02	-	0.16	<0.01	0.82	1.00
2-1	0.61	-	16.05	0.10	64.07	18.60	99.43	0.02	-	0.42	<0.01	0.55	1.00
2-2	0.56	0.09	13.73	0.12	67.69	17.91	100.10	0.02	<0.01	0.38	<0.01	0.60	1.00
2-3	0.55	-	12.47	0.13	68.85	17.55	99.55	0.02	-	0.35	<0.01	0.63	1.00
2-4	0.50	-	9.70	0.11	72.67	16.71	99.69	0.02	-	0.29	<0.01	0.70	1.00
2-5	0.46	-	8.69	0.11	73.68	16.45	99.39	0.02	-	0.26	<0.01	0.72	1.00
2-6	0.45	0.09	7.84	0.11	74.84	16.37	99.71	0.02	<0.01	0.24	<0.01	0.74	1.01
2-7	0.46	-	7.47	0.11	75.40	16.15	99.58	0.02	-	0.23	<0.01	0.75	1.00
2-8	0.41	-	7.12	0.08	75.67	15.92	99.19	0.02	-	0.22	<0.01	0.76	1.00
2-9	0.45	-	6.39	0.11	76.84	15.71	99.50	0.02	-	0.20	<0.01	0.78	1.00
2-10	0.38	-	5.45	0.08	78.71	15.25	99.86	0.01	-	0.17	<0.01	0.82	0.99

847 Note: the analyses for both crystals are given in descending order of zinc content from the crystal core to

848 the rim.

849

This is the peer-reviewed, final accepted version for American Mineralogist, published by the Mineralogical Society of America.
The published version is subject to change. Cite as Authors (Year) Title. American Mineralogist, in press.
DOI: https://doi.org/10.2138/am-2025-9783. http://www.minsocam.org/

850 **Table 3.** Trace-element composition (ppm) of zoned metacinnabar grains, LA-ICP-MS data.

Element	1	2	3	4	5	6	7	8	9	10
	V3 (Fig. 4a)	V3 (Fig. 4a)	V3 (Fig. 4a)	V3 (Fig. 4a)	V3 (Fig. 4a)	VK38v (Fig. 4b)	VK38v (Fig. 4b)	Vk38v (Fig. 3c)	Vk38v (Fig. 3c)	Vk38v (Fig. 3c)
Zn, wt%*	24.9	22.4	17.8	16.1	9.0	15.5	8.5	9.5	8.5	6.2
Mn	8470	6750	6870	8100	5500	6890	5160	4420	3457	2710
Fe	772	1243	714	677	375	698	427	323	229	162
Cu	159	238	1360	118	77	60.9	30	520	520	111
Ga	1.38	1.1	1.71	1.26	1.46	2.44	1.7	1.26	1.13	1.4
As	1600	350	2350	500	240	57	1200	368	486	1500
Se	13	26	26.4	49	70	51	101	52	60	122
Ag	bdl	0.18	0.35	0.074	bdl	bdl	0.087	0.129	0.086	0.071
Cd	2224	2480	1976	2074	1710	2014	1661	1481	1391	1705
In	51.7	54.2	52.0	56.2	32.7	50.3	30.5	33.3	28.7	22.1
Sn	2.4	1.93	2.02	1.71	2.32	1.7	3.11	1.46	0.61	1.53
Sb	118	196	1250	124	42	7.7	44	227	720	179
Te	11.7	11.1	27.1	18.2	54	13.5	88	56	69	175
Au	bdl	bdl	0.155	bdl	0.029	bdl	0.13	0.152	bdl	0.106
Tl	210	430	3770	148	114	25.7	11.3	640	1140	330
Pb	0.58	3.54	17.7	3.1	0.53	bdl	0.36	0.29	43.4	3.71
Bi	0.041	bdl	0.41	bdl	bdl	bdl	bdl	bdl	0.66	0.058

851 *EPMA data used for calculation LA-ICP-MS data; bdl – below detection limit. Ablation profiles
852 segments of 50–100 μm length were used for compositions calculations. Note: an. 1–2 correspond to the
853 Hg-enriched sphalerite core (Sp1) and an. 3–10 to Zn-enriched metacinnabar (Mcin2).

854

This is the peer-reviewed, final accepted version for American Mineralogist, published by the Mineralogical Society of America.
The published version is subject to change. Cite as Authors (Year) Title. American Mineralogist, in press.
DOI: https://doi.org/10.2138/am-2025-9783. http://www.minsocam.org/

Figure 1

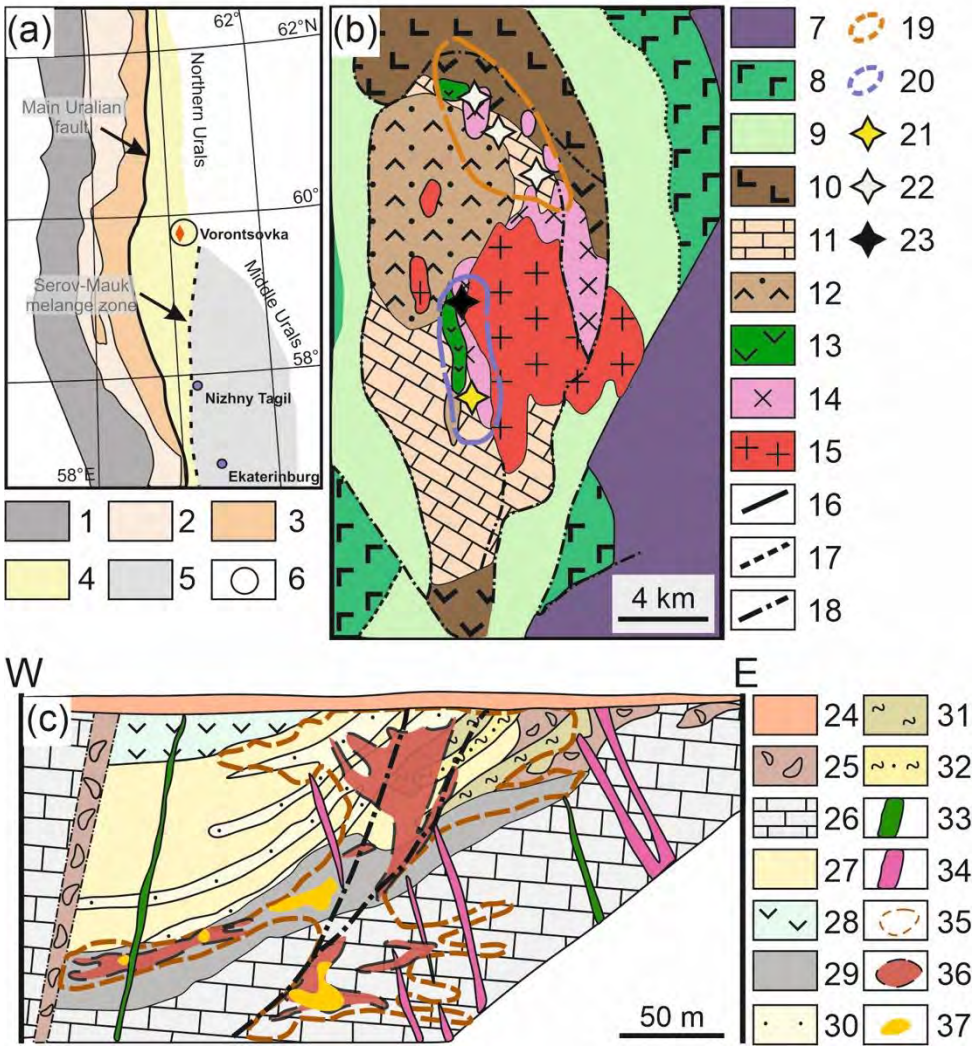

855
856

This is the peer-reviewed, final accepted version for American Mineralogist, published by the Mineralogical Society of America.
The published version is subject to change. Cite as Authors (Year) Title. American Mineralogist, in press.
DOI: https://doi.org/10.2138/am-2025-9783. http://www.minsocam.org/

Figure 2

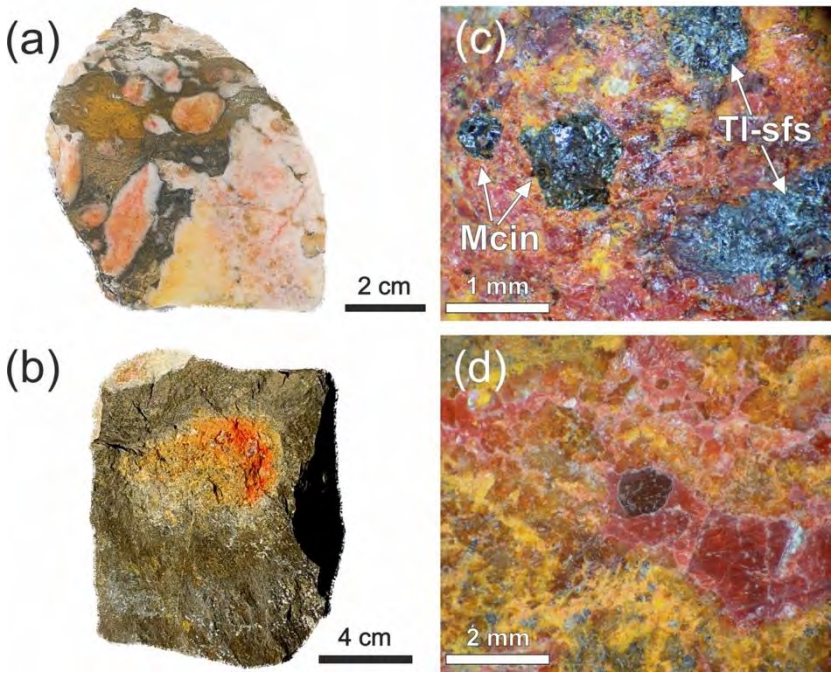

857

This is the peer-reviewed, final accepted version for American Mineralogist, published by the Mineralogical Society of America.
The published version is subject to change. Cite as Authors (Year) Title. American Mineralogist, in press.
DOI: https://doi.org/10.2138/am-2025-9783. http://www.minsocam.org/

Figure 3

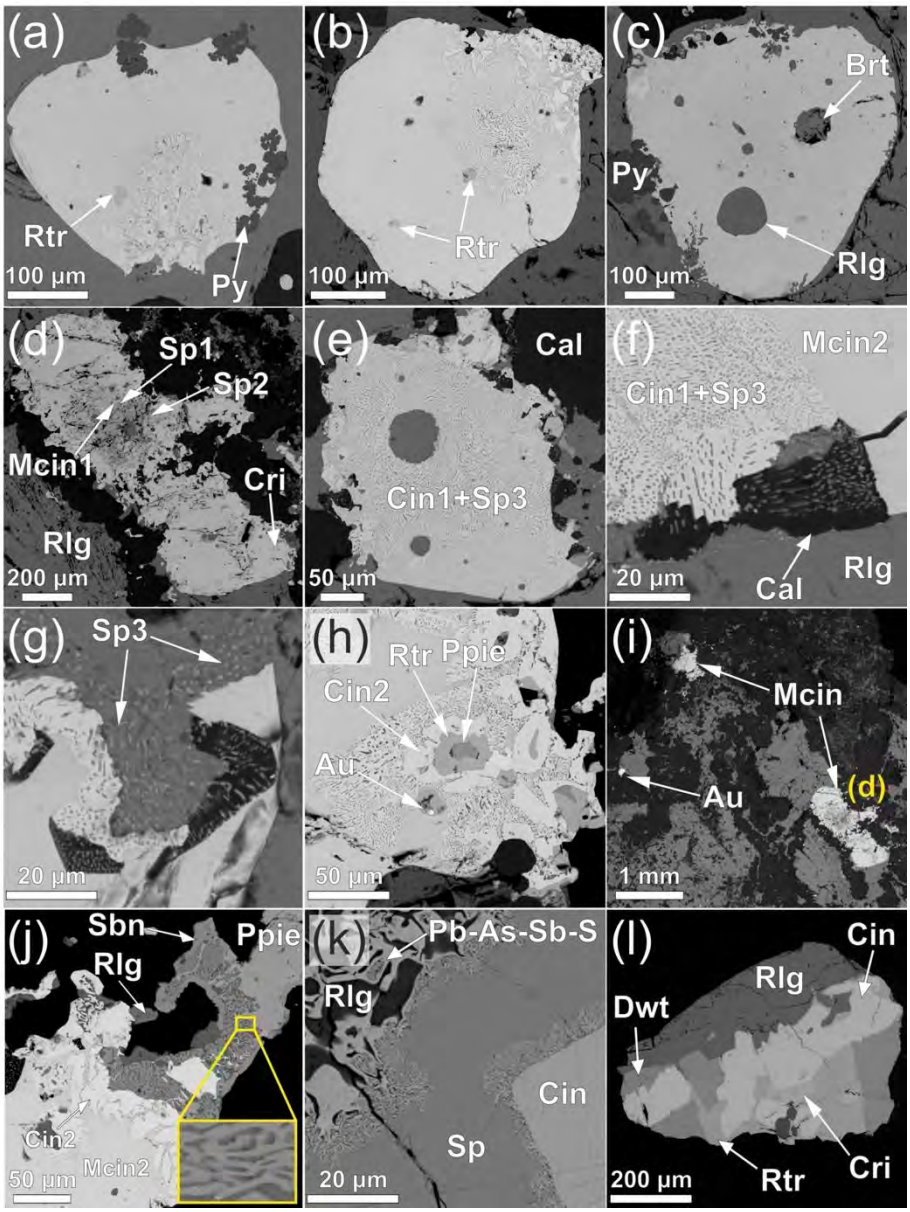

This is the peer-reviewed, final accepted version for American Mineralogist, published by the Mineralogical Society of America.
The published version is subject to change. Cite as Authors (Year) Title. American Mineralogist, in press.
DOI: https://doi.org/10.2138/am-2025-9783. http://www.minsocam.org/

Figure 4

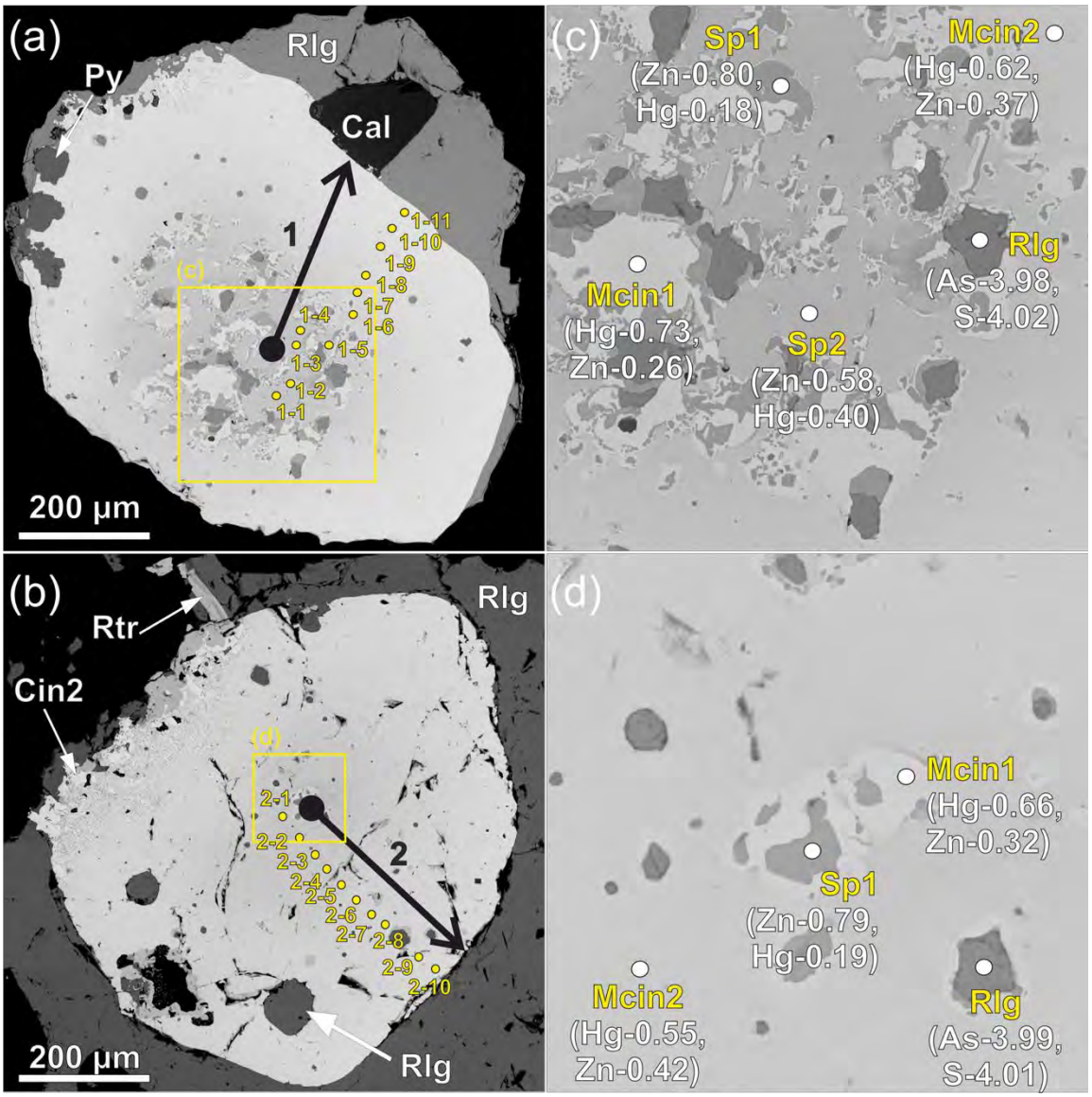

This is the peer-reviewed, final accepted version for American Mineralogist, published by the Mineralogical Society of America.
The published version is subject to change. Cite as Authors (Year) Title. American Mineralogist, in press.
DOI: https://doi.org/10.2138/am-2025-9783. http://www.minsocam.org/

Figure 5

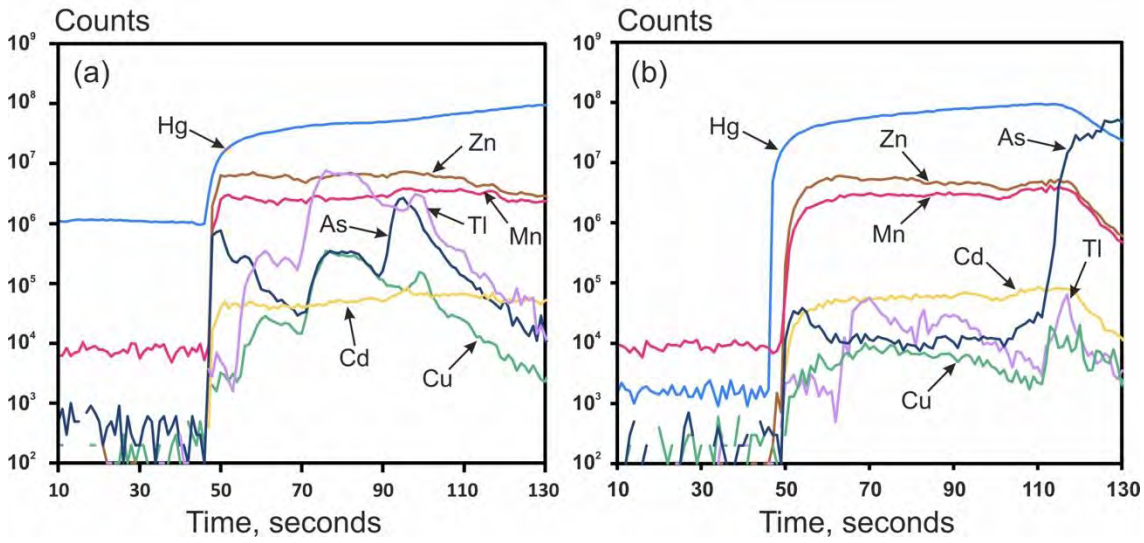

Figure 6

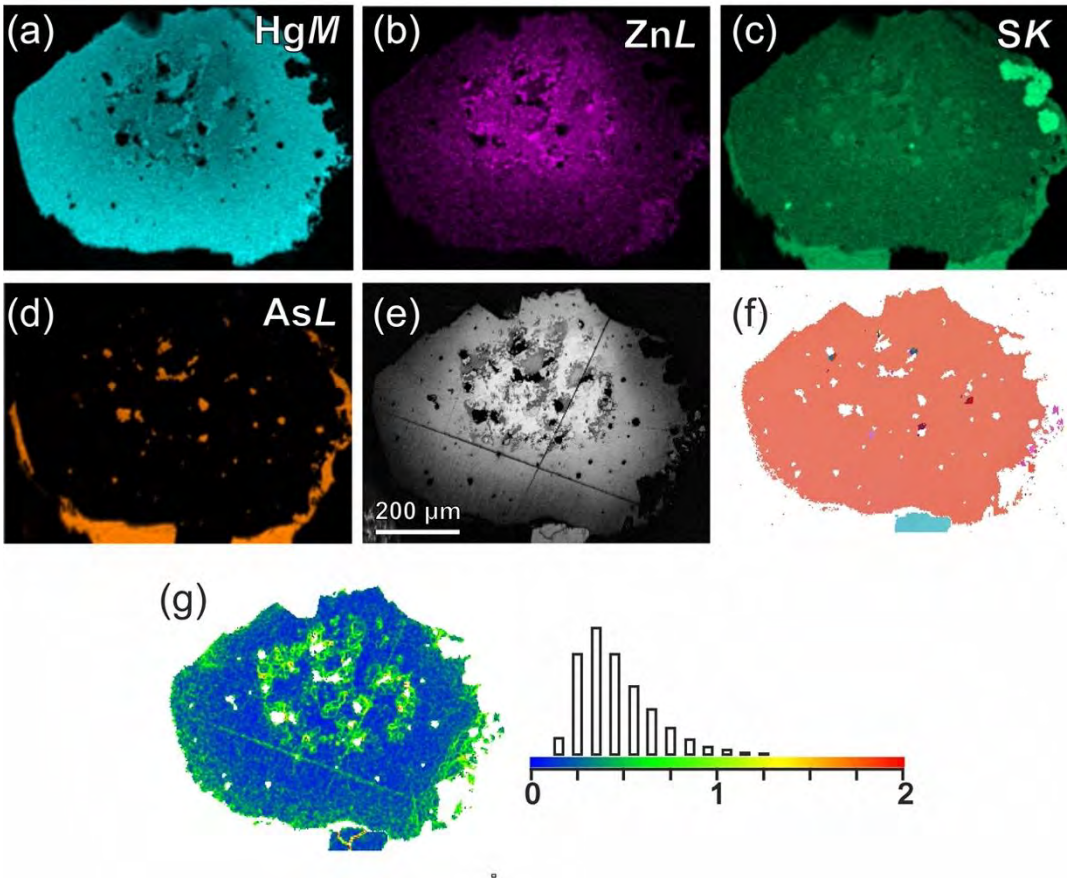

This is the peer-reviewed, final accepted version for American Mineralogist, published by the Mineralogical Society of America.
The published version is subject to change. Cite as Authors (Year) Title. American Mineralogist, in press.
DOI: https://doi.org/10.2138/am-2025-9783. http://www.minsocam.org/

Figure 7

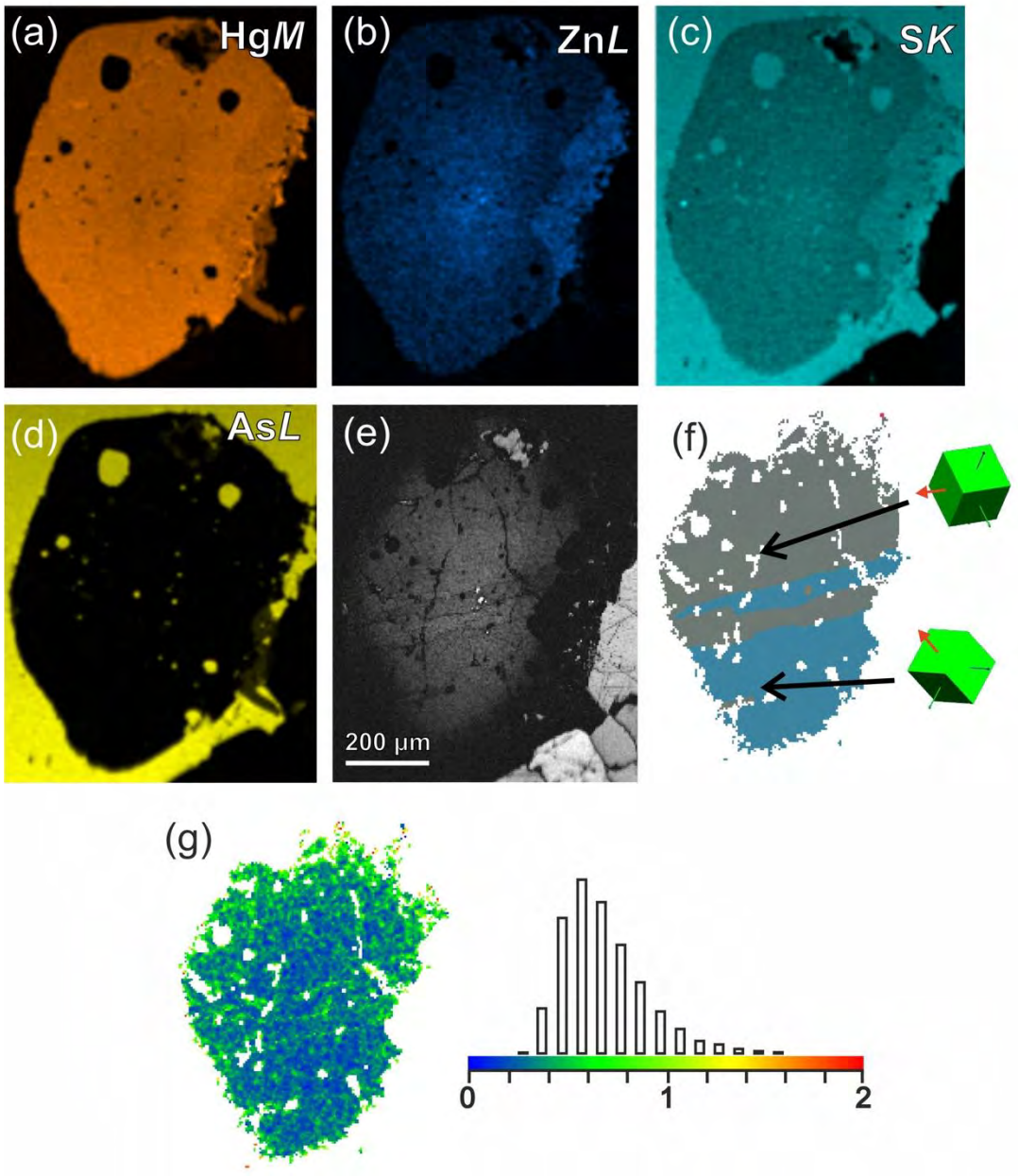

869
870

This is the peer-reviewed, final accepted version for American Mineralogist, published by the Mineralogical Society of America.
The published version is subject to change. Cite as Authors (Year) Title. American Mineralogist, in press.
DOI: https://doi.org/10.2138/am-2025-9783. http://www.minsocam.org/

Figure 8

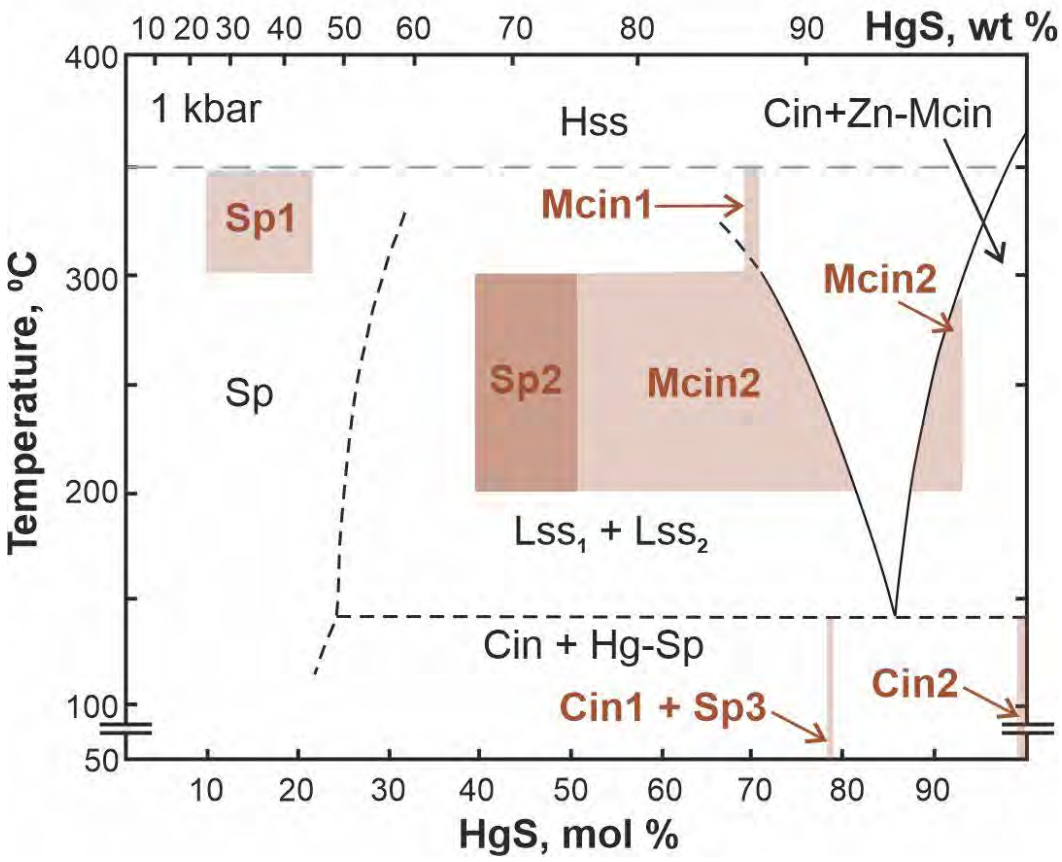

871
872

This is the peer-reviewed, final accepted version for American Mineralogist, published by the Mineralogical Society of America.
The published version is subject to change. Cite as Authors (Year) Title. American Mineralogist, in press.
DOI: https://doi.org/10.2138/am-2025-9783. http://www.minsocam.org/

Figure 9

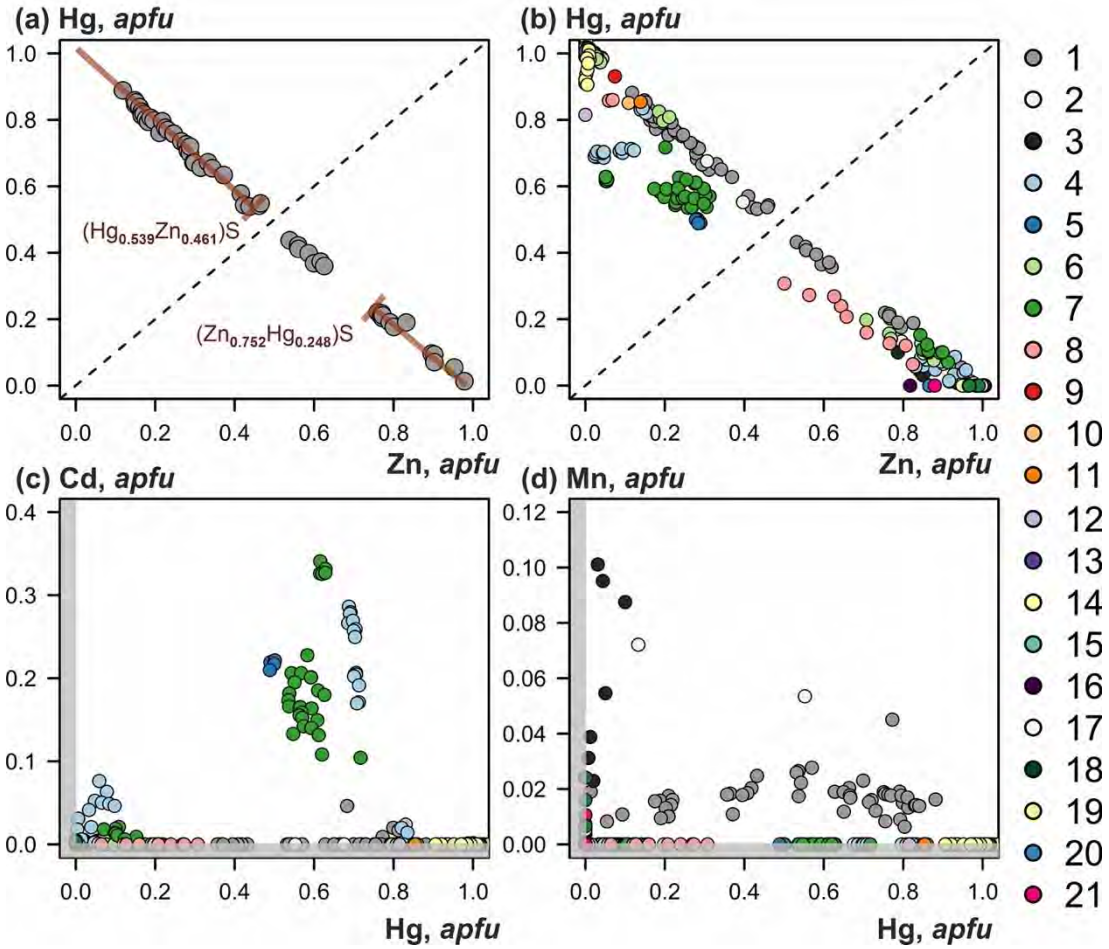

873

874

This is the peer-reviewed, final accepted version for American Mineralogist, published by the Mineralogical Society of America.
The published version is subject to change. Cite as Authors (Year) Title. American Mineralogist, in press.
DOI: https://doi.org/10.2138/am-2025-9783. http://www.minsocam.org/

Figure 10

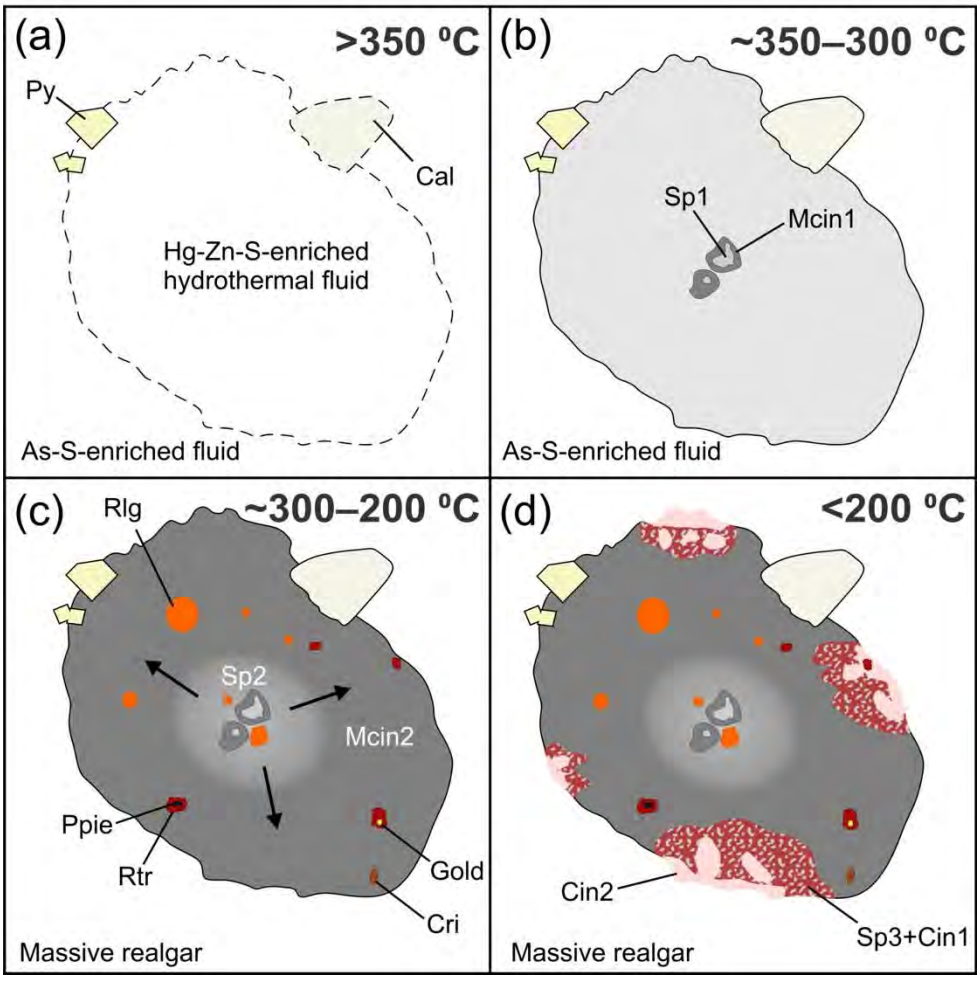

875